Title

Robust effects of cloud superparameterization on simulated daily rainfall intensity statistics across multiple versions of the Community Earth System Model

Journal

Journal of Advances in Modeling Earth Systems, 8(1)

ISSN

1942-2466

Authors

Kooperman, Gabriel J
Pritchard, Michael S
Burt, Melissa A
et al.

Publication Date

2016-03-01

DOI

10.1002/2015ms000574

Peer reviewed

AGU PUBLICATIONS

Journal of Advances in Modeling Earth Systems

RESEARCH ARTICLE

10.1002/2015MS000574

Key Points:
- Superparameterization improves the rainfall amount mode and extreme rates relative to TRMM 3B42
- Mean rainfall and dry day frequency biases do not improve much with superparameterization
- Conventional and superparameterized rainfall intensity statistics are similar poleward of 50°

Supporting Information:
- Supporting Information S1

Correspondence to:
G. J. Kooperman,
gkooperm@uci.edu

Citation:
Kooperman, G. J., M. S. Pritchard, M. A. Burt, M. D. Branson, and D. A. Randall (2016), Robust effects of cloud superparameterization on simulated daily rainfall intensity statistics across multiple versions of the Community Earth System Model, *J. Adv. Model. Earth Syst.*, *8*, 140–165, doi:10.1002/2015MS000574.

Received 28 OCT 2015
Accepted 29 DEC 2015
Accepted article online 2 JAN 2016
Published online 1 FEB 2016

Robust effects of cloud superparameterization on simulated daily rainfall intensity statistics across multiple versions of the Community Earth System Model

Gabriel J. Kooperman[1], Michael S. Pritchard[1], Melissa A. Burt[2], Mark D. Branson[2], and David A. Randall[2]

[1]Department of Earth System Science, University of California, Irvine, California, USA, [2]Department of Atmospheric Science, Colorado State University, Fort Collins, Colorado, USA

Abstract This study evaluates several important statistics of daily rainfall based on frequency and amount distributions as simulated by a global climate model whose precipitation does not depend on convective parameterization—Super-Parameterized Community Atmosphere Model (SPCAM). Three superparameterized and conventional versions of CAM, coupled within the Community Earth System Model (CESM1 and CCSM4), are compared against two modern rainfall products (GPCP 1DD and TRMM 3B42) to discriminate robust effects of superparameterization that emerge across multiple versions. The geographic pattern of annual-mean rainfall is mostly insensitive to superparameterization, with only slight improvements in the double-ITCZ bias. However, unfolding intensity distributions reveal several improvements in the character of rainfall simulated by SPCAM. The rainfall rate that delivers the most accumulated rain (i.e., amount mode) is systematically too weak in all versions of CAM relative to TRMM 3B42 and does not improve with horizontal resolution. It is improved by superparameterization though, with higher modes in regions of tropical wave, Madden-Julian Oscillation, and monsoon activity. Superparameterization produces better representations of extreme rates compared to TRMM 3B42, without sensitivity to horizontal resolution seen in CAM. SPCAM produces more dry days over land and fewer over the ocean. Updates to CAM's low cloud parameterizations have narrowed the frequency peak of light rain, converging toward SPCAM. Poleward of 50°, where more rainfall is produced by resolved-scale processes in CAM, few differences discriminate the rainfall properties of the two models. These results are discussed in light of their implication for future rainfall changes in response to climate forcing.

1. Introduction

Rainfall is an intrinsic characteristic of a region's climate, by definition determining whether the region is a desert or rainforest [*Peel et al.*, 2007]. As the Earth warms, global mean precipitation is expected to increase by 1–3% $°C^{-1}$ due to radiative constraints [*Allen and Ingram*, 2002; *Pendergrass and Hartmann*, 2014a; *Stephens and Ellis*, 2008], but regional changes are much less robust [*Dai*, 2006; *Mahlstein et al.*, 2012; *Stocker et al.*, 2013]. Regional rainfall is driven over time by changes in circulation, moisture transport, and local evaporation [*Trenberth et al.*, 2003]. These changes can depend on complex interactions between rainfall, large-scale dynamics, and surface sensible and latent heat fluxes, especially over land where soil moisture coupling plays an important role [*Seneviratne et al.*, 2010]. Interactions linked to the second-order statistics of rainfall (e.g., frequency and intensity) can determine whether rain is intercepted by the canopy, infiltrates the soil, or runs off the surface, thus influencing the soil moisture [*Lawrence et al.*, 2011; *Ramirez and Senarath*, 2000]. In turn, the soil moisture effects local evaporation and sensible heat fluxes, which project onto large-scale dynamics and downstream moisture transport [*Dirmeyer et al.*, 2009; *Koster et al.*, 2004; *Seneviratne et al.*, 2010]. These second-order rainfall characteristics are expected to change even more than the mean, up to ~7% $°C^{-1}$ on global scales, and even larger on regional scales [*O'Gorman*, 2015; *Trenberth et al.*, 2003]. For these reasons, and because rainfall frequency and intensity control the prevalence of devastating drought or flood conditions, it is critical they be realistically simulated in global climate models (GCMs).

While GCMs simulate mean rainfall patterns reasonably well [*Dai*, 2006], they have substantial frequency and intensity biases, most notably a tendency to rain too weakly and too often [*Sun et al*., 2006; *O'Gorman and Schneider*, 2009]. To a large degree these biases are associated with the limitations of convective parameterizations, but progress has also been hindered by a lack of observational constraints to evaluate these statistics on global-spatial and daily-time scales; differences among observational products can be as large as model biases [*Liu and Allan*, 2012]. Despite these biases and limited assessment, GCMs are often used to investigate the sensitivity of rainfall intensity statistics to climate forcings or large-scale variability directly [*Pendergrass and Hartmann*, 2014b, 2014c] or by scaling (observationally constraining) climate change projections with observed present-day rainfall variability [*O'Gorman*, 2012]. However, given the complexity of radiative and dynamic feedbacks important to precipitation processes [*Seager et al*., 2010], and the range of uncertainty across individual GCMs [*Dai*, 2006; *Sun et al*., 2006], capturing the baseline representation of precipitation may be a first-order requirement for capturing the climate change response. Models that are unable to realistically simulate present-day rainfall intensity statistics may be incompletely representing important mechanisms driving precipitation changes.

In many ways it is not a surprise that GCMs fail to capture second-order rainfall statistics. The convective parameterizations used in most GCMs are formulated to balance large-scale thermal instabilities, not drive small-scale microphysical and precipitation processes [*Arakawa and Schubert*, 1974; *Zhang and McFarlane*, 1995]. Precipitation is thus a diagnostic consequence of large-scale instability and the convective response rather than a prognostic part of the formulation. Mean rainfall is constrained by the necessary latent heating required by the atmosphere, but the space-time scales over which this constraint is applied are limited by horizontal resolution and subjective parameter settings (e.g., convective time scale) [*Gustafson et al*., 2014]. From the perspective of convective parameterization, realistic rainfall intensity is not energetically necessary; the same mean latent heating from infrequent intense events can be produced from frequent weak events. Only in an explicit representation of convection is the rainfall rate interactively coupled to the large-scale energetics of the system. This is one reason simulated rainfall intensity improves when GCMs are run at higher resolution, and more rainfall is produced by resolved-scale processes relative to parameterizations [*Kopparla et al*., 2013].

However, for global-scale climate-length simulation, explicit cloud-resolving resolution is computationally impractical, and there are few alternatives to the conventional convective parameterization framework. A computationally appealing alternative, evaluated here, which permits cloud-scale convective processes, is called cloud superparameterization. In the superparameterization approach, simplified high-resolution ($\sim$4 km) cloud-resolving models embedded in a conventional GCM replace convective cloud and boundary layer parameterizations (e.g., *Randall et al*. [2003] described in more detail below). Recent evaluations of this approach have shown skill in capturing important modes of convective variability including mesoscale convection systems [*Pritchard et al*., 2011; *Kooperman et al*., 2013, 2014], African Easterly Waves [*McCrary et al*., 2014], the Madden-Julian oscillation [*Benedict and Randall*, 2009], the Asian Monsoon [*DeMott et al*., 2011], and the El Niño Southern Oscillation [*Stan et al*., 2010]. This has led to regional improvements in the diurnal timing [*Khairoutdinov et al*., 2005; *Pritchard and Somerville*, 2009a, 2009b] and intensity of rainfall during summer at several ground sites [*DeMott et al*., 2007] and over much of the United States [*Li et al*., 2012; *Rosa and Collins*, 2013]. Mean rainfall analysis has shown mixed results, with a possible improvement in the double-ITCZ (Inter-Tropical Convergence Zone) bias in one version [*Stan et al*., 2010], but a tropical Indian and West Pacific wet bias in other versions [*Khairoutdinov et al*., 2005]. Potential version sensitivities have also been noted in the improved diurnal cycle in SPCAM [*Marchand and Ackerman*, 2010; *Pritchard et al*., 2011]. There has yet to be a full assessment of rainfall mean and intensity statistics across multiple versions of the superparameterized CAM.

The primary aim of this paper is to fill this gap; comparing simulated rainfall produced by two very different ways of representing global-scale atmospheric convection. We have not attempted a full assessment of all available rainfall observations here, but focus instead on differences between conventional and superparameterization. Descriptions of the models used are provided in section 2, along with a summary of two widely used observational precipitation products analyzed here for reference, and details of our analysis methodology. The results are summarized in section 3, and the conclusions and future work are discussed in section 4.

2. Background

2.1. Methods

2.1.1. Rainfall Distributions

The analysis here focuses on several statistics of daily rainfall based on frequency and amount distributions. Together these distributions reveal the rain rates that occur most often and those that contribute the most accumulated rain. The distributions of observed and simulated rainfall are based on histograms with discrete rain rate bins, which can be constructed and visualized in many ways (e.g., linear [*Chou et al*., 2012; *Sun et al*., 2007], logarithmic [*Hennessy et al*., 1997; *Pendergrass and Hartmann*, 2014b, 2014c], gamma [*Watterson and Dix*, 2003], etc.). The choice of bin spacing may be motivated by many factors including an attempt to represent the nature of the convention generating the rainfall [*Panorska et al*., 2007], emphasize extreme events at the tail of the distribution [*Cavanaugh et al*., 2015], or form a distribution that can easily be operated on mathematically [*Pendergrass and Hartmann*, 2014b, 2014c]. The choice determines (1) the spacing between bins, (2) the width of each bin, and (3) the minimum rain rate (i.e., dry day threshold for nonlinear spacing). Ideal bin structure will fully sample all observed and simulated rain rates and provide a quasi-continuous estimate that is representative of the true population.

In this study, we do not assess all possible mathematical models that could fit the precipitation distribution; there is already a long history of literature on the subject evaluating distributions over a wide variety of space-time scales. Here logarithmic bin spacing is applied for global-scale GCM analysis following the methodology of *Pendergrass and Hartmann* [2014b], which offers several demonstrated advantages: it is a mathematically continuous function, each bin center and width is a fixed percentage larger than the previous bin, and it can capture the full range of rain rates across orders of magnitude. These features make the distribution easy to operate on and interpret, especially when also visualized in a logarithmic coordinate system. In this system the bin spacing and width are related to each other by a fixed percentage. *Pendergrass and Hartmann* [2014b, 2014c] used 7% spacing to draw a connection to the theoretical 7% °C increase of rainfall intensity associated with the Clausius-Clapeyron humidity response to temperature change [*Held and Soden*, 2006; *Trenberth*, 2011]. They included all rain rates greater than 0.03 mm d^{-1}, defining a *dry day threshold* as days with less accumulated rain.

Here a slightly larger 10% spacing is used for simplicity and to reduce noise in distributions created from the short (5–10 year) analysis periods and the coarse (∼1–2°) exterior horizontal resolutions of the simulations. A dry day threshold of 0.1 mm d^{-1} is used (as in *Chou et al*. [2012] and *Sun et al*. [2007]), such that all days with accumulated rain greater than 0.1 mm d^{-1} are considered rainy, and the first rainy bin includes rates between 0.1 and 0.11 mm d^{-1} (i.e., bin edges), centered on 0.105 mm d^{-1} with a bin width of 0.01 mm d^{-1}. This structure yields a relationship with bin centers 10X larger than their width, so that approximate bin centers 1, 10, 100, and 1000 mm d^{-1} have approximate bin widths of 0.1, 1, 10, and 100 mm d^{-1}, respectively, with nearly 100 bins between 0.1 and 1000 mm d^{-1} (4 orders of magnitude).

Distributions are constructed from accumulated daily rainfall (r, units of mm d^{-1}) at each grid point independently before calculating area-weighted averages globally and for various regions of interest (e.g., land-only, tropics, etc.). Discrete forms of the frequency (f) and amount distributions (p) are given by:

$$f_i\left(R_i^c\right)=\frac{1}{\Delta \ln R}\frac{1}{N_T}\sum N\left(R_i^l \le r < R_i^r\right), \tag{1}$$

$$p_i\left(R_i^c\right)=\frac{1}{\Delta \ln R}\frac{1}{N_T}\sum r\left(R_i^l \le r < R_i^r\right), \tag{2}$$

where i represents each bin, R_i^c are bin centers with edges R_i^l and R_i^r, N is the number of days, N_T is the total number of days, bin width $\Delta \ln R = \Delta R/R = 0.1$, and the distributions are related to each other by approximately:

$$p\left(R_i^C\right)=f\left(R_i^C\right)R_i^C. \tag{3}$$

Rain rate percentiles are calculated from the cumulative frequency distribution:

$$F_i\left(R_i^c\right)=\sum_0^i f_i\left(R_i^c\right)\Delta \ln R, \tag{4}$$

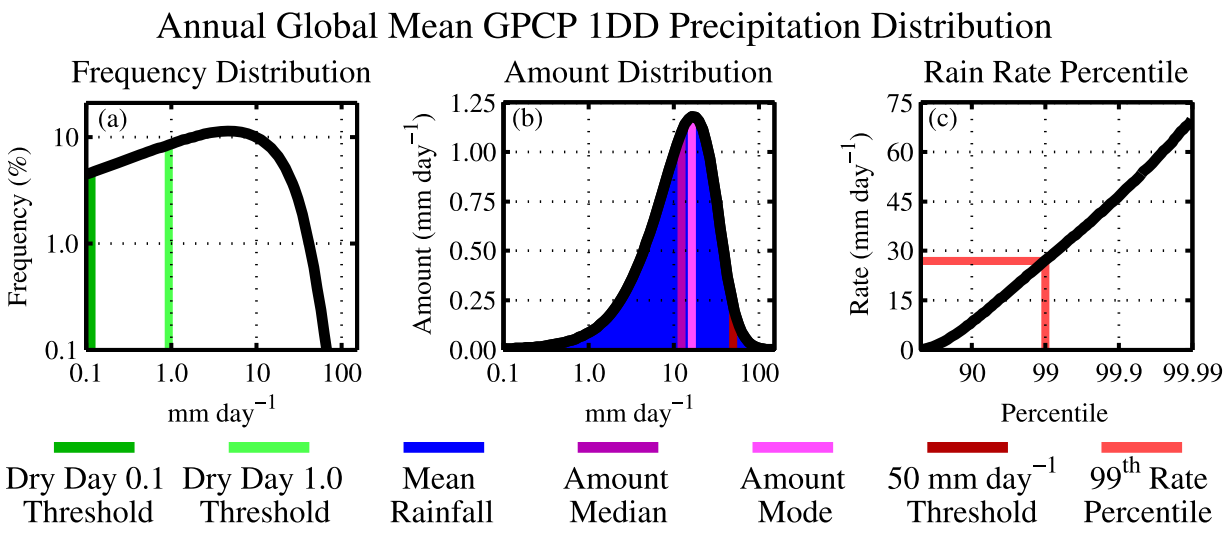

Figure 1. Precipitation (a) frequency distribution (%), (b) amount distribution (mm d^{-1}), and (c) percentile precipitation rates (mm d^{-1}) from global annual GPCP 1DD daily precipitation.

including all dry and rainy days, where the 99th percentile rain rate is the value of R interpolated to $F=0.99$. The frequency and amount distributions are visualized on a logarithmic rain rate x axis to graphically depict bin spacing consistent with the bin structure. The frequency distribution is visualized on a logarithmic frequency y axis and the rain rate percentiles are visualized on a logarithmic reduction percentile x axis to help discriminate the extreme tails of the distribution. An example of these three plots constructed from 10 years of global annual daily precipitation at ~1° resolution (0.9° × 1.25°) is shown in Figure 1.

When depicted in a logarithmic coordinate system the dry day frequency (i.e., the percent of days with rain rates below 0.1 mm d^{-1}) is not shown (Figure 1a). Since half of grid point days in the global average are not raining, a significant percentage (~51%, see Table 2) of the frequency distribution is not shown. For the rainy bins shown, the peak rain rate frequency is less than 10 mm d^{-1} and drops off at higher rain rates. The peak in the amount distribution (Figure 1b) is shifted to the right compared to the frequency distribution, more than 10 mm d^{-1}, because lower rain rates do not contribute as much accumulated daily rainfall. In fact, rain rates below 1 mm d^{-1} contribute little overall rainfall, though they occur frequently. The rain rate percentiles (Figure 1c) highlight the extreme tail of the frequency distribution, which in the global average, represents rain rates that occur infrequently both in space (e.g., Tropical West Pacific and Inter-Tropical Convergence Zone regions) and in time (e.g., convective clusters and tropical cyclones).

Together these three plots illustrate several important characteristics of observed and simulated rainfall including: mean rainfall, dry day frequency, extreme rainfall intensity, and rainfall amount mode. A brief overview of these characteristics and their calculation is provided here:

Mean rainfall is depicted in Figure 1b as the integral of the area under the curve of the amount distribution (blue shading) in units of mm d^{-1}. This can be calculated directly from the distribution as $\sum p\Delta \ln R$ or independently for each grid point and area-averaged, providing validation that the bin structure covers the full range of rain rates and the dry day threshold does not cutoff appreciable accumulated rain. Mean rainfall results are discussed in section 3.2 below.

Dry day frequency is calculated as the number of days to the left of the vertical green lines in the frequency distribution (Figure 1a), including completely dry days (<0.1 mm d^{-1}) that are not shown on the log-scale. We evaluate dry day frequency using two threshold values, 0.1 and 1.0 mm d^{-1}. The first (0.1 mm d^{-1}) is the value used in the construction of the distributions and includes all times defined as not raining. From the amount distribution (Figure 1b), it is clear that rain rates below this value do not contribute much accumulated rain. For comparison, a larger threshold (1.0 mm d^{-1}) is also used to accommodate the limitations of both satellite measurements, which struggle to observe low rain rates, and conventional GCM simulations, which tend to rain too weakly and too often. A larger threshold is often used to account for both the satellite and model deficiencies [*Polade et al.*, 2014]. Dry day frequency can be calculated directly from the distribution (including completely dry days not shown in the plots), or independently by simply summing

the number of days with accumulated rain less than the threshold value, and therefore does not depend on discrete bin spacing. Dry day frequency results are discussed in section 3.3 below.

Extreme rainfall intensity is evaluated using the 99th percentile rain rate and the total accumulated rain from rates above 50 mm d^{-1}, as shown by the red lines in Figures 1b and 1c, respectively. As above, these statistics can be calculated directly from the distributions or independently from the raw rainfall data, and thus do not depend on the choice of discrete bin structure. Extreme rainfall intensity results are discussed in section 3.4 below.

Rainfall amount mode represents the rain rate that delivers the most accumulated rainfall, and is given by the peak in the amount distribution, depicted as the light purple line in Figure 1b. This is a subtle statistic that depends on both the frequency that a particular rain rate occurs and the actual value of that rain rate. It is the rain rate that produces the most surface reaching rainfall, and thus has particular importance for the hydrological cycle. It can only be calculated from the distribution, and is therefore somewhat sensitive to the choice of bin structure and spacing. However, the sign of the bias result (if the simulated amount mode is too weak or too heavy compared to observations) is robust to this choice. A complementary metric, the amount median, depicted as the dark purple line in Figure 1b, is also evaluated. The amount median is the rain rate where half the accumulated rain comes from rates below and above its value, and unlike the mode, can be calculated independently from the distribution. The amount mode and median results are discussed in section 3.5 below.

2.2. Observations

The objective of this paper is to evaluate the influence of superparameterization on rainfall statistics relative to conventional convective parameterization. Two widely used observational data products are analyzed here to benchmark the simulations, one from the Global Precipitation Climatology Project (GPCP) [*Huffman et al*., 2001, 2012a] and one from the Tropical Rainfall Measuring Mission (TRMM) [*Huffman et al*., 2007, 2012b]. We have found that these two products, though both extensively used in previous model evaluation studies [e.g., *Allan et al*., 2014; *Pendergrass and Hartmann*, 2014b, 2014c; *Pritchard and Somerville*, 2009a, 2009b; *Rasch et al*., 2006], provide very different estimates of "truth" for many of the statistics presented below. It is outside the scope of this analysis to conduct a detailed observational intercomparison, or state with any expertise which product is more trustworthy. Both products are included as a means of bracketing the range of possible observational estimates, and their differences are noted in the results alongside the simulations. We provide a brief description of these data products below, and highlight known differences in the measurement techniques that lead us to trust one more than the other for certain statistics. The comparison between observations and model simulations presented in our results also indicate reasons to trust one product more than the other as described in discussion, but again this paper is not an observational intercomparison and the authors are not experts in remote sensing. We encourage collaboration between the observation and modeling communities to provide a more detailed and thorough evaluation of these statistics.

GPCP provides a daily estimate of accumulated precipitation gridded globally at 1° resolution called the One-Degree Daily (1DD) Precipitation Data Set version 1.2, hereafter referred to simply as GPCP 1DD [*Huffman et al*., 2001, 2012a]. The data are provided by the National Aeronautics and Space Administration (NASA) Goddard Space Flight Center (GSFC) and are available for download from their website (ftp://rsd.gsfc.nasa.gov/pub/1dd-v1.2/). Within the region from 40°S to 40°N, daily rainfall is estimated from infrared (IR) measurements made onboard geosynchronous and low earth orbit satellites, which are compiled at 1° horizontal resolution every 3 hours. The precipitation rate is aggregated daily from the IR data using a Threshold-Matched Precipitation Index (TMPI) constrained by monthly Special Sensor Microwave Imager (SSM/I) and GPCP version 2 satellite-gauge precipitation data [*Huffman et al*., 1997, 2001]. Poleward of 40° the Television and Infrared Observation Satellite (TIROS) Operational Vertical Sounder (TOVS) Pathfinder Path A data set provides an estimate of daily precipitation calculated from retrievals of cloud and surface properties [*Susskind et al*., 1997]. The regions are merged across 40° to form the 1DD product using spatial smoothing, and the daily rainfall estimate is scaled to match monthly GPCP satellite-gauge data. For more details, see *Huffman et al*. [2001].

TRMM data are used in a 3 hourly instantaneous precipitation estimate gridded between 50°S and 50°N at 0.25° resolution known as the Multi-satellite Precipitation Analysis (TMPA) product 3B42 version 7, here after referred to simply as TRMM 3B42 [*Huffman et al*., 2007, 2012b]. The data are provided by the NASA GSFC

Table 1. Annual Mean Precipitation With 95% Confidence Interval (mm d^{-1})[a]

Region	GPCP 1DD	TRMM 3B42	CCSM4	SPCCSM4	CESM1 CAM4	SPCESM1 CAM4	CESM1 CAM5	SPCESM1 CAM5
90°S–90°N	2.65 ± 0.03		2.99 ± 0.01	2.85 ± 0.02	2.86 ± 0.03	2.91 ± 0.02	3.03 ± 0.02	2.88 ± 0.02
^{L}90°S–90°N	2.14 ± 0.03		2.42 ± 0.02	2.02 ± 0.02	2.24 ± 0.06	2.06 ± 0.05	2.18 ± 0.02	2.23 ± 0.08
^{O}90°S–90°N	2.87 ± 0.03		3.23 ± 0.01	3.19 ± 0.02	3.12 ± 0.02	3.25 ± 0.02	3.38 ± 0.03	3.15 ± 0.03
50°S–50°N	2.89 ± 0.03	2.91 ± 0.03	3.30 ± 0.01	3.16 ± 0.02	3.19 ± 0.03	3.25 ± 0.03	3.41 ± 0.03	3.20 ± 0.02
^{L}50°S–50°N	2.55 ± 0.04	2.52 ± 0.04	2.88 ± 0.02	2.37 ± 0.03	2.70 ± 0.10	2.45 ± 0.07	2.66 ± 0.03	2.72 ± 0.11
^{O}50°S–50°N	3.01 ± 0.03	3.05 ± 0.04	3.45 ± 0.01	3.43 ± 0.02	3.35 ± 0.02	3.53 ± 0.02	3.67 ± 0.04	3.37 ± 0.03
90°S–50°S	2.01 ± 0.06		2.09 ± 0.03	1.96 ± 0.02	1.97 ± 0.05	1.93 ± 0.03	2.01 ± 0.02	2.06 ± 0.02
50°S–15°S	2.42 ± 0.02	2.14 ± 0.05	2.59 ± 0.03	2.58 ± 0.03	2.46 ± 0.05	2.67 ± 0.04	2.69 ± 0.03	2.68 ± 0.08
15°S–15°N	3.99 ± 0.05	4.35 ± 0.04	4.89 ± 0.05	4.54 ± 0.04	4.74 ± 0.12	4.67 ± 0.07	5.04 ± 0.08	4.64 ± 0.12
15°N–50°N	2.22 ± 0.03	2.22 ± 0.03	2.36 ± 0.02	2.31 ± 0.02	2.27 ± 0.02	2.33 ± 0.02	2.40 ± 0.04	2.21 ± 0.02
50°N–90°N	1.76 ± 0.05		1.89 ± 0.02	1.74 ± 0.02	1.74 ± 0.03	1.75 ± 0.02	1.72 ± 0.04	1.72 ± 0.06

[a]Superscripts L and O denote land-only and ocean-only averaging regions, respectively.

Mirador website (http://mirador.gsfc.nasa.gov). The 3B42 algorithm combines visible, IR, and microwave radiometer measurements from the TRMM satellite with precipitation measurements from other satellite products into a single calibrated, gap-filled, 3 hourly estimate. The 3 hourly precipitation rate is then calibrated and scaled to match monthly Global Precipitation Climatology Center (GPCC) rain gauge data. Here 3 hourly instantaneous values are further averaged to produce a daily estimate consistent with GPCP 1DD. The TRMM 3B42 product has shown skill in capturing the histogram of precipitation rates relative to surface observations in several regions (see *Huffman et al*. [2007] for more details).

There is substantial literature of observational studies using these data products to assess statistics of rainfall intensity, a brief summary of relevant results is provided here:

Mean rainfall estimated from long time integrations over large regions of gridded measurements are fairly consistent (2.89 ± 0.03 and 2.91 ± 0.03 mm d^{-1} over 50°S–50°N annually for GPCP 1DD and TRMM 3B42, respectively, see Table 1), but the products are less certain and can be inconsistent at the subpentad time scale due to issues associated with the averaging of input data streams [*Liu and Allan*, 2012]. However, some studies indicate that daily rainfall from TRMM 3B42 may be more reliable than GPCP 1DD (e.g., the Continental United States [*Alemohammad et al*., 2015]) because it contains more microwave radiometer input streams [*Rossow et al*., 2013], which in turn are known to validate well against ground-based radar constraints [*Wolff and Fisher*, 2009].

Dry day frequency is sensitive to the subjective threshold chosen to define rainy versus dry days, and is especially uncertain when the chosen cutoff falls within the light drizzle range [*Polade et al*., 2014]. Very light drizzle (represented by a small peak in the frequency distribution) is often missing in gridded rainfall products, perhaps due to issues associated with microwave retrievals at low rain rates [*Liu and Allan*, 2012]. As a result, the drizzle peak seen in some models (*Pendergrass and Hartmann* [2014b, 2014c] call it the "light rain mode") is not present in the GPCP 1DD or TRMM 3B42 distributions, but is validated by merged products that emphasize CloudSAT's enhanced observations in this regime [*Behrangi et al*., 2012], not analyzed here.

Table 2. Annual Dry Day Frequency With 95% Confidence Interval (%)[a]

Region	GPCP 1DD	TRMM 3B42	CCSM4	SPCCSM4	CESM1 CAM4	SPCESM1 CAM4	CESM1 CAM5	SPCESM1 CAM5
90°S–90°N	51.0 ± 0.5		25.9 ± 0.1	25.6 ± 0.6	23.6 ± 0.2	23.2 ± 0.2	19.8 ± 0.1	22.7 ± 0.1
^{L}90°S–90°N	57.6 ± 0.8		39.8 ± 0.2	53.0 ± 0.4	40.0 ± 0.3	52.7 ± 0.3	41.5 ± 0.6	46.3 ± 0.2
^{O}90°S–90°N	48.3 ± 0.4		20.1 ± 0.2	14.4 ± 0.7	16.9 ± 0.3	11.2 ± 0.3	10.9 ± 0.1	13.1 ± 0.2
50°S–50°N	53.1 ± 0.3	53.3 ± 0.9	27.5 ± 0.1	25.5 ± 0.7	24.6 ± 0.3	22.7 ± 0.3	18.3 ± 0.2	22.2 ± 0.2
^{L}50°S–50°N	59.1 ± 0.5	56.9 ± 0.5	41.2 ± 0.3	55.7 ± 0.5	41.3 ± 0.5	56.3 ± 0.5	41.1 ± 1.0	48.3 ± 0.4
^{O}50°S–50°N	51.0 ± 0.3	52.0 ± 1.2	22.6 ± 0.2	14.9 ± 0.7	18.7 ± 0.3	11.0 ± 0.4	10.3 ± 0.2	13.1 ± 0.3
90°S–50°S	41.8 ± 1.9		19.0 ± 0.1	21.8 ± 0.6	18.9 ± 0.3	21.0 ± 0.4	20.7 ± 0.3	20.3 ± 0.0
50°S–15°S	56.2 ± 0.4	59.5 ± 1.3	26.8 ± 0.3	22.0 ± 0.7	22.6 ± 0.6	18.1 ± 0.3	14.9 ± 0.5	15.8 ± 0.8
15°S–15°N	43.6 ± 0.4	42.0 ± 0.7	17.9 ± 0.1	16.0 ± 0.7	15.9 ± 0.2	13.8 ± 0.7	9.5 ± 0.4	15.1 ± 0.3
15°N–50°N	59.7 ± 0.3	58.7 ± 0.9	38.0 ± 0.4	38.8 ± 0.6	35.6 ± 0.4	36.8 ± 0.7	30.9 ± 0.8	36.0 ± 0.6
50°N–90°N	46.8 ± 1.3		22.5 ± 0.5	29.7 ± 0.3	22.5 ± 0.9	28.7 ± 0.4	28.1 ± 0.5	28.3 ± 1.0

[a]Superscripts L and O denote land-only and ocean-only averaging regions, respectively.

Extreme rainfall intensity is likely to be underestimated in both GPCP 1DD and TRMM 3B42 products relative to the direct satellite measurements that go into them [*Liu and Allan*, 2012], but there is some evidence that TRMM 3B42 is better able to capture extreme rain when compared to gauge data (e.g., over Malaysia [*Tan et al*., 2015] and East Africa [*Dinku et al*., 2011]). A better measurement of extremes in TRMM 3B42 would be consistent with its assimilation of a wide ensemble of independent satellite passive microwave constraints, which distinguishes it from GPCP 1DD. However, while many studies have found more extreme rainfall in TRMM 3B42 compared to GPCP 1DD [*Liu and Allan*, 2012; *Dinku et al*., 2011; *Tan et al*., 2015], others have found the reverse [*Rossow et al*., 2013], suggesting the analysis can be sensitive to methodology, data product versions, and location. The estimation of rainfall intensity can also be sensitive to horizontal resolution and whether dry days are included in its estimation [*Rossow et al*., 2013], making it difficult to cross-compare different studies.

Rainfall amount mode has been studied in observations [e.g., *Wolff and Fisher*, 2009; *Rossow et al*., 2013; *Tan et al*., 2015; *Behrangi et al*., 2012], but has not been a major focus of climate model evaluation (though recently commented on by *Pendergrass and Hartmann* [2014b]) because large mean state biases (e.g., double-ITCZ) remain the first-order problem. Unlike extreme rain, the amount mode is less sensitive to the horizontal scale of observations [*Behrangi et al*., 2012]. Between the two products, the amount mode estimate in Table 5 from TRMM 3B42 (26.4 mm d^{-1}) is a better match than GPCP 1DD (18.0 mm d^{-1}) when compared to multiple observational products, including CloudSat, as reported in *Behrangi et al*. [2012].

2.3. Models

In this study, we analyze rainfall from three conventional and superparameterized (SP) versions of the Community Atmosphere Model (CAM). CAM is the atmospheric component of the fully coupled (interactive atmosphere, land, ocean, and sea ice) Community Earth System Model version 1 (CESM1), formally the Community Climate System Model version 4 (CCSM4). Two versions of CAM are available within CESM1, CAM version 4 (CAM4), and CAM version 5 (CAM5); CAM4 is also coupled within CCSM4. When CESM1 is run with CAM4 physics (CESM1-CAM4) it uses many of the same components and parameterizations as CCSM4. Both CCSM4 and CESM1 use the same base versions of the Community Land Model version 4 (CLM4), the Parallel Ocean Program version 2 (POP2), and the Community Ice CodE version 4 (CICE4). For more details on each of these components, see *Lawrence et al*. [2011] for CLM4, *Smith et al*. [2010] for POP2, and *Hunke and Lipscomb* [2008] for CICE4. A much larger change in the atmospheric component is represented by the step from CAM4 to CAM5 in CESM1, which updates the convective and microphysical cloud parameterizations. Below we provide a brief description of CAM and highlight differences between model versions. For more details on the fully coupled system see *Gent et al*. [2011] and for scientific descriptions of CAM4 and CAM5 see *Neale et al*. [2010a, 2010b].

For each version of CAM, we compare a superparameterized counterpart (SPCAM). Superparameterization, including differences between model versions, is described in more detail below. To make the comparison clear, the following naming convention is used to denote the different model versions. We will use "CAM" and "SPCAM" as shorthand classifiers for results relevant to all three versions, but the actual conventional and superparameterized realizations of each of the three versions are defined as (SP)CCSM4, (SP)CESM1-CAM4, and (SP)CESM1-CAM5, referring to individual models CCSM4 and SPCCSM4, CESM1-CAM4 and SPCESM1-CAM4, and CESM1-CAM5 and SPCESM1-CAM5, respectively. We analyze three versions of each model class here to discriminate robust effects of superparameterization across versions (i.e., SPCAM versus CAM), and to isolate differences associated with the atmospheric model (i.e., (SP)CESM1-CAM4 versus (SP)CESM1-CAM5, only the atmosphere model changes between these versions) from the fully coupled system (i.e., (SP)CCSM4 versus (SP)CESM1-CAM4).

2.3.1. Community Atmosphere Model

CAM is a three-dimensional global atmospheric general circulation model that has been widely used for climate research for over twenty years. CAM development has been led by the National Center for Atmospheric Research (NCAR) with support from National Science Foundation (NSF) and Department of Energy (DOE), and in collaboration with multiple NSF, DOE, and academic laboratories. Versions 4 and 5 used here are run with a finite volume dynamical core that solves the hydrostatic equations of motion on a fixed horizontal grid and terrain-following hybrid vertical coordinate [*Neale et al*., 2010a, 2010b]. Unresolved vertical fluxes of mass and energy driven by subgrid deep convection are approximated by ensembles of convective updraft plumes formulated to consume convective available potential energy [*Zhang and McFarlane*,

1995]. In CAM4, modifications were added to this scheme [*Neale et al*., 2010a] to include dilution of the ascending plumes by entrainment mixing [*Raymond and Blyth*, 1992] and the vertical transport of horizontal momentum by convection [*Richter and Rasch*, 2008].

CAM5 uses the same deep convection scheme, but introduces a new shallow convection formulation [*Park and Bretherton*, 2009] designed to improve low cloud radiative feedbacks through moist turbulent processes [*Bretherton and Park*, 2009]. These updates link to a two-moment cloud microphysics formulation that independently tracks liquid and ice cloud condensate mass and number concentrations [*Morrison and Gettelman*, 2008]. Cloud condensate in the microphysics scheme are activated from aerosol particles represented by a three-mode module that includes internal mixtures of fifteen aerosol constituents distributed into Aitken, accumulation, and coarse modes [*Liu et al*., 2012]. Aerosol-cloud and radiation interactions feed into radiative transfer calculations through the Rapid Radiative Transfer Model for GCMs (RRTMG), a major update from the radiative transfer parameterizations used in CAM4 [*Neale et al*., 2010b; *Iacono et al*., 2008]. For details on these parameterizations and differences between versions see *Neale et al*. [2010a, 2010b].

2.3.2. Superparameterization

Cloud superparameterization has become a mature technique for simulating atmospheric convection and cloud processes, and is now a true alternative to conventional parameterizations, viable for global climate length simulations. It has been implemented in the latest version of CESM and is available for public download via the NCAR CESM development subversion code repository (https://www2.cgd.ucar.edu/sections/cseg/development-code). The implementation of superparameterization in CAM has been led by the NSF Science and Technology Center for Multiscale Modeling of Atmospheric Processes (www.cmmap.org) with recent collaboration between Pacific Northwest National Laboratory and NCAR. The approach is now also available in several other community modeling frameworks including the Weather Research and Forecast model [*Tulich*, 2015], the Integrated Forecasting System (M. Khairoutdinov, personal communication, 2015), the Max Planck Institute for Meteorology ECHAM GCM (H. Tost, personal communication, 2015), and the NASA Goddard GCM [*Tao et al*., 2009]. Similar methods of "superparameterization" are expanding into other aspects of earth system modeling as well, including simulating deep convective processes in the ocean [*Campin et al*., 2011].

Unlike most GCMs that use statistical methods to represent unresolved subgrid moist convection approximately, cloud superparameterization uses embedded cloud-resolving models (CRMs) to represent it explicitly, replacing the conventional convective and boundary layer parameterizations used in CAM [*Randall et al*., 2003]. In this framework, two scale regimes are simultaneously resolved, outer large-scale dynamics resolved on the GCM grid, and inner cloud-scale physics permitted by a high-resolution CRM array [*Grabowski*, 2001; *Khairoutdinov and Randall*, 2001]. The CRMs are configured as independent two-dimensional arrays with periodic boundaries relaxed toward large-scale tendencies within each GCM grid-column, which return array-mean cloud properties and convective tendencies to the GCM [*Benedict and Randall*, 2009]. The CRM is the System for Atmospheric Modeling described in detail in *Khairoutdinov and Randall* [2003], but which has also evolved over time in each version of SPCAM (M. Khairoutdinov, personal communication, 2015). SPCAM is about a hundred times more computer intensive than a normal GCM, but scales efficiently on large parallel computers, and is now practical for multidecadal simulations using current supercomputing technology [e.g., *Pritchard and Bretherton*, 2014]. Although the computational overhead of superparameterization can now be reduced substantially using acceleration techniques [*Pritchard et al*., 2014; *Jones et al*., 2015], these approaches are not employed in any of the SPCAM simulations analyzed here.

Most of the differences between CAM versions discussed above also extend to their SPCAM counterparts. The major updates from SPCCSM4 and SPCESM1-CAM4 to SPCESM1-CAM5 involve the implementation of two-moment cloud microphysics and its links to more sophisticated aerosol processes [*Wang et al*., 2011]. The modal aerosol module in CAM5 is active in SPCESM1-CAM5 and interacts with cloud processes on the CRM-scale through the Explicit Cloud Parameterized Pollutants (ECPP) module [*Gustafson et al*., 2008]. The aerosol fields are tracked at the GCM-scale and updated based on distributions of convective updraft velocity and cloud properties across the CRM-array, but cloud droplet activation and radiative transfer is calculated independently for each CRM column based on local conditions. Cloud droplet activation feeds into the liquid portion of a two-moment microphysics scheme in the CRM, which tracks liquid and ice number and mass concentrations [*Morrison et al*., 2005]. For more details about SPCAM in general see *Khairoutdinov and Randall* [2001], and for SPCESM-CAM5 specific updates see *Wang et al*. [2011]. A detailed description

and evaluation of the fully coupled SPCAM is available for the SPCCSM4 version, provided by *Stan and Xu* [2014].

2.4. Simulations and Configurations

Though SPCAM is now computationally affordable on advanced supercomputing infrastructure, climate length simulations still remain at the cutting edge of current capabilities. The simulations evaluated here are some of the longest ever made with fully coupled versions of SPCAM. As a result, the simulations were designed to facilitate multiple studies, and there are some differences in the configuration and setup between model versions. However, each CAM-SPCAM pair has a consistent GCM-scale configuration and simulation setup. And there are common configurations between all six simulations including: a finite volume dynamical core for the atmosphere, a horizontal resolution of the land surface corresponding with the atmosphere, and a consistent 1° horizontal resolution for the ocean and sea-ice. Differences in configuration and simulation setup are described below, which we view not as limitations, but rather as useful parameter space to sample toward identifying robust effects of cloud superparameterization.

The (SP)CCSM4 simulations were configured with a GCM horizontal resolution of 0.9° latitude by 1.25° longitude (referred to here after as 1°) and 30 vertical levels. These simulations were run as climate change projections for the 21st century forced by the Representative Concentration Pathway 8.5 (RCP8.5) emissions scenario [*Taylor et al*., 2012]. In this study, the first 10 years (2006–2015) are analyzed as representative of present-day conditions. The CRM in SPCCSM4 was run with 32 columns at 3 km horizontal resolution in an east-west orientation, and 28 vertical levels corresponding with the bottom 28 levels in CAM. Output from these simulations is available via the Earth System Grid (www.earthsystemgrid.org), and more details on CCSM4 and SPCCSM4 can be found in *Gent et al*. [2011] and *Stan and Xu* [2014], respectively.

The (SP)CESM1-CAM4 and (SP)CESM1-CAM5 simulations were configured with a GCM horizontal resolution of 1.9° latitude by 2.5° longitude (referred to here after as 2°) and 30 vertical levels. These simulations were run with constant preindustrial greenhouse gas concentrations and external forcings for 10 years. They were branched from initial conditions generated by long climatologically stable preindustrial simulations with conventional versions of CAM. Since initializing SPCAM from CAM conditions in this way can introduce drift toward SPCAM's unique climatological state, especially for slow developing soil moisture fields in the land model, only the last 5 years for these simulations are analyzed here. In addition to the difference in GCM-scale resolution, the CRMs in SPCESM1-CAM4 and SPCESM1-CAM5 were also configured differently than SPCCSM4. In these runs the CRMs had 32 columns at 4 km horizontal resolution in a north-south orientation, and 28 vertical levels.

For the results presented in section 3 below, both observational rainfall products were independently mapped to each model grid using area conserving spatial interpolation. The closest 10 year overlap period was used for the observational analysis (2004–2013) to match the (SP)CCSM4 simulations (2006–2015), though there is no expectation that the models would reproduce the observed time series of large-scale modes of variability. Ten year averaging periods for the observations and (SP)CCSM4 simulations were used to examine present-day climatological conditions, and 5 year averaging periods for (SP)CESM1-CAM4 and (SP)CESM1-CAM5 simulations were used to analyze preindustrial conditions. We acknowledge that these are short periods to represent "climatology," so will focus our discussion on results that are robust across all model versions and over large geographic regions.

3. Results

3.1. Rainfall Distributions

As in Figure 1 described above, Figure 2 analyzes rainfall distributions of frequency (top), amount (middle), and percentile rates (bottom) from GPCP 1DD (black), TRMM 3B42 (gray), CAM (red), and SPCAM (blue) in versions (SP)CCSM4 (left), (SP)CESM1-CAM4 (center), and (SP)CESM1-CAM5 (right). In Figure 2, only grid points within the TRMM 3B42 observed region (50°S–50°N) are included for both models and observations. GPCP 1DD and TRMM 3B42 observations were regridded to two horizontal resolutions corresponding to different model versions: 1° for comparison to (SP)CCSM4 (left) and 2° for comparison to (SP)CESM1-CAM4 and (SP)CESM1-CAM5 (center and right). The horizontal resolution naturally affects statistics of the gridded rainfall products, for instance at higher resolution the observed distributions capture more extreme rain rates

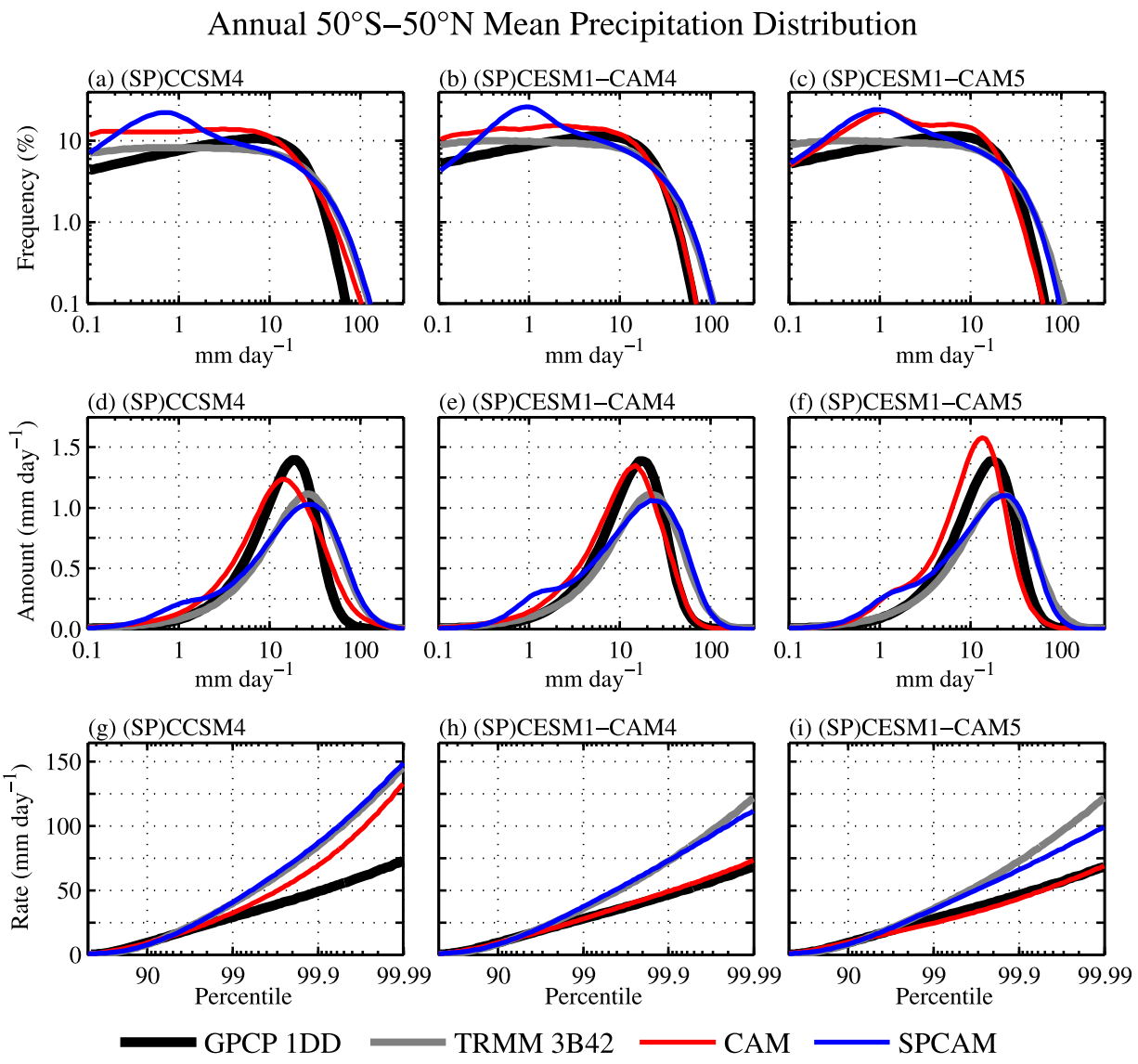

Figure 2. Precipitation (a, b, c) frequency distribution (%), (d, e, f) amount distribution (mm d^{-1}), and (g, h, i) percentile precipitation rates (mm d^{-1}) from annual GPCP 1DD, TRMM 3B42, (a, d, g) (SP)CCSM4, (b, e, h) (SP)CESM1-CAM4, and (c, f, i) (SP)CESM1-CAM5 daily precipitation averaged from 50°S to 50°N; GPCP 1DD and TRMM 3B42 are shown at 1° resolution in comparison to (SP)CCSM4 and 2° resolution in comparison to (SP)CESM1-CAM4 and (SP)CESM1-CAM5.

than the lower resolution. This effect can be seen by comparing the TRMM 3B42 99.99th percentile value in Figure 2g, which reaches 150 mm d^{-1}, to Figures 2h and 2i, for which the 99.99th percentile value in the same TRMM 3B42 product reaches only 125 mm d^{-1}, a consequence of regridding.

To unfold geographic variations in the statistics of daily rainfall, the same distributions analyzed in Figure 2 are shown in Figure 3, but only for grid points with greater than 50% of the model's internal land fraction. Figure 4 further unfolds the latitude dependence of the amount distribution into five zonal average regions, where 50°S–15°S, 15°S–15°N, and 15°N–50°N each represent about 25% of Earth's surface area, and together 90°S–50°S and 50°N–90°N represent the remaining 25%. Taken together, Figures 2–4 reveal important characteristics and differences of observed and simulated rainfall, and discriminate the role of the tropics versus midlatitudes and ocean versus land in contributing to the total distribution.

In the frequency distributions (Figures 2a–2c) there are systematic differences in the rainfall observed by GPCP 1DD and TRMM 3B42, where TRMM 3B42 estimates a higher frequency of more intense rates that drop off smoothly rather than peaking at a moderate rate (~10 mm d^{-1}) as they do in GPCP 1DD. For rain rates greater than 10 mm d^{-1}, these two observational estimates are as different from each other as they

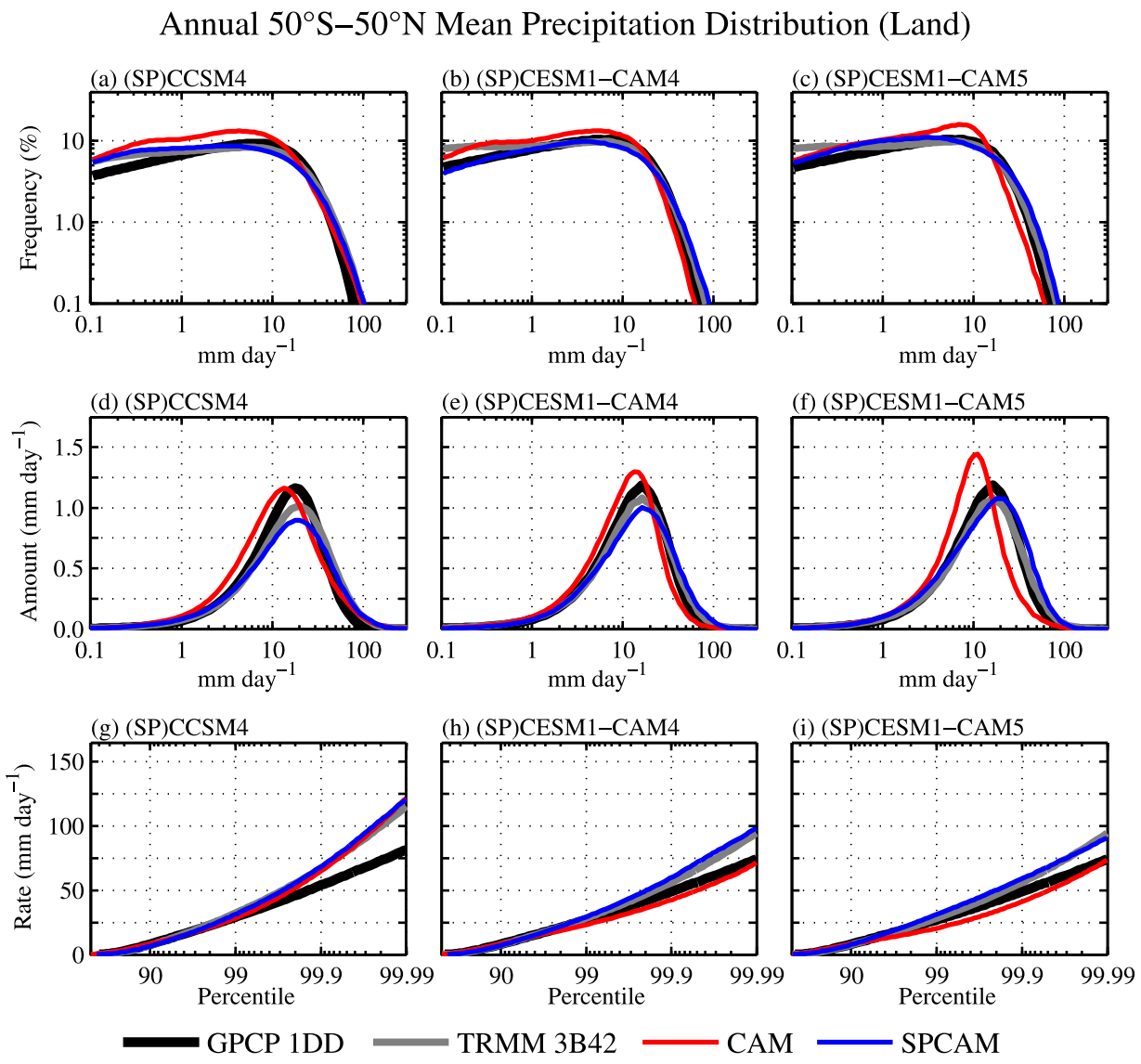

Figure 3. Precipitation (a, b, c) frequency distribution (%), (d, e, f) amount distribution (mm d^{-1}), and (g, h, i) percentile precipitation rates (mm d^{-1}) from annual GPCP 1DD, TRMM 3B42, (a, d, g) (SP)CCSM4, (b, e, h) (SP)CESM1-CAM4, and (c, f, i) (SP)CESM1-CAM5 daily precipitation averaged for land-only from 50°S and 50°N; GPCP 1DD and TRMM 3B42 are shown at 1° resolution in comparison to (SP)CCSM4 and 2° resolution in comparison to (SP)CESM1-CAM4 and (SP)CESM1-CAM5.

are from the model results. In all three versions, SPCAM is nearly identical to TRMM 3B42 at higher rates (greater than 5 mm d^{-1}) and captures the frequency of the most intense rates observed by TRMM 3B42, while CAM is a much better match to the GPCP 1DD estimate, simulating a moderate peak and less frequent occurrence of intense rates. However, CAM shows greater version and resolution dependence, with the higher-resolution CCSM4 version better capturing the intensity of TRMM 3B42 and SPCAM.

For light rain rates, both CAM and SPCAM tend to simulate higher occurrence than either observational estimate. This appears to be due to a simulated drizzle mode over the ocean that is not seen in either observational product. In the land-only distributions (Figure 3) this mode largely disappears, especially in SPCAM, and both models and observations are more consistent. Though over land, the lower-resolution versions of CAM maintain an unrealistic moderate rain rate peak and continue to miss the most intense observed rates.

However, the character of the oceanic drizzle mode is different between the two models, with a narrow light rain peaked (0.8–1 mm d^{-1}) simulated by SPCAM (Figures 1a–1c, blue lines), which is missing in early versions of CAM (Figures 1a and 1b, red lines), but is evident in CESM1-CAM5 (Figure 1c, red line). Though this light rain peak is not represented in the observations, it could be a promising improvement in the

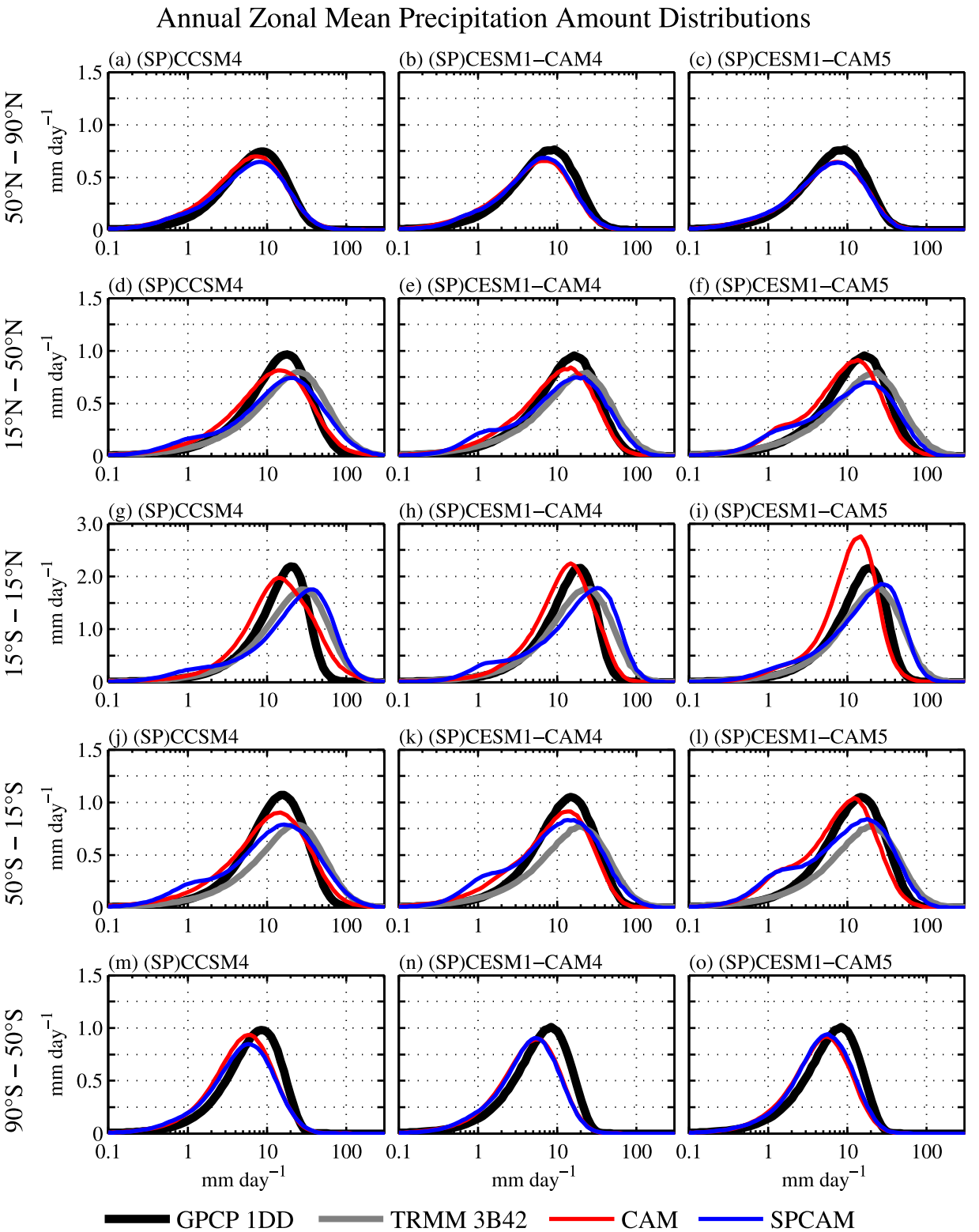

Figure 4. Precipitation amount distributions from (a, b, c) 50°N to 90°N, (d, e, f) 15°N to 50°N, (g, h, i) 15°S to 15°N, (j, k, l) 50°S to 15°S, and (m, n, o) 90°S to 50°S zonal averages for annual GPCP 1DD, TRMM 3B42, (a, d, g, j, m) (SP)CCSM4, (b, e, h, k, n) (SP)CESM1-CAM4, and (c, f, i, l, o) (SP)CESM1-CAM5 daily precipitation; GPCP 1DD and TRMM 3B42 are shown at 1° resolution in comparison to (SP)CCSM4 and 2° resolution in comparison to (SP)CESM1-CAM4 and (SP)CESM1-CAM5.

evolution of CAM4 to CAM5, with parameterized solutions beginning to converge to superparameterized solutions. When using CAM4 physics, this distinct drizzle mode is not present and the model produces nearly uniform frequency for all rain rates less than ~8 mm d^{-1}, including frequent very light drizzle (less than 0.2 mm d^{-1}), a familiar problem in legacy versions of CAM. Parameterization updates in CESM1-CAM5 capture the missing drizzle mode peak and reduce very light drizzle. In fact, the parameterized version of CESM1-CAM5 strongly resembles the superparameterized version for rates below 3 mm d^{-1}. This suggests that new shallow convection parameterizations in CESM1-CAM5 produce effects comparable to cloud superparameterization at light rain rates, at a fraction of the expense.

Although the drizzle mode is the dominant peak in the frequency distribution, it does not contribute much to accumulated surface precipitation, and thus is only subtly visible in the amount distribution as a small left shoulder in all versions of SPCAM (blue lines) and CAM version CESM1-CAM5 (red line) in Figures 2d–2f. Only a small fraction of accumulated rain falls at rates less than 3 mm d^{-1} and we therefore shift attention to the rest of the rainfall distribution, in which there are systematic differences in GPCP 1DD versus TRMM 3B42 and CAM versus SPCAM, across model versions. These differences can appear subtle from the perspective of the frequency distributions (Figures 2a–2c), but are quite clear in the amount distributions (Figures 2d–2f). Consistent with the frequency distributions, the amount distributions demonstrate that TRMM 3B42 estimates significantly more rain from more intense rain rates than GPCP 1DD. The amount distributions also demonstrate that SPCAM results are very consistent with TRMM 3B42, while CAM results are more consistent with GPCP 1DD. Like TRMM 3B42, the SPCAM distribution includes a significant amount of accumulated surface rainfall from high rates, even heavier than 100 mm d^{-1}. The higher-resolution CAM version CCSM4 is able to simulate some extreme rain at the right tail of the distribution, but not nearly as much accumulated rain as is observed by TRMM 3B42 and simulated by SPCAM.

However, the most striking difference in the amount distribution is the peak, or "amount mode," which represents the rain rate that delivers the most accumulated rainfall. The amount mode in GPCP 1DD is significantly weaker than TRMM 3B42 when the oceans are included, but over land (Figures 3d–3f), where both observational estimates are better constrained by surface measurements, the observed distributions collapse onto each other. In all versions, the SPCAM amount mode is a better match to observations over land (Figures 3d–3f), and TRMM 3B42 over oceans and land (Figures 2d–2f). CAM, on the other hand, systematically predicts a lower amount mode (~10–20 mm d^{-1}) than GPCP 1DD, TRMM 3B42, and SPCAM (~20–40 mm d^{-1}), over both land and ocean. And despite the fact that the higher-resolution CAM version CCSM4 is able to capture more extreme rain, it does not improve the amount mode. The systematic underestimation of the amount mode thus seems to clearly encapsulate a symptom of an ongoing bias in CAM's deep convection parameterization—it is unable to capture the heavy intensity of the majority of storms that deliver accumulated global rainfall. This appears to be systematically improved with superparameterization, if one assumes that the TRMM 3B42 daily rainfall product's distribution is a more reliable observational proxy than GPCP 1DD.

The mode of the amount distribution is an especially physical quantity, since it represents the rain rate that delivers the most accumulated rainfall. Therefore, its simulated discrepancies are worth understanding in more detail. One limitation of the above analysis, which includes all grid points from 50°S to 50°N, is that the amount distribution is dominated by the tropics, where most accumulated rainfall occurs. To reveal potentially interesting model differences occurring elsewhere, Figure 4 thus regionalizes the analysis of the amount distribution to independent latitude bands. This confirms that the essence of the problem seen in Figures 2 and 3 stems from the tropics; in 15°S–15°N, the amount mode is underestimated in CAM by a factor of 2–3 relative to SPCAM (Figures 4g–4i). Elsewhere, the superparameterized and conventionally parameterized rainfall distributions are in better agreement. In fact, poleward of 50° latitude, the amount distribution is remarkably insensitive to whether convection is parameterized or superparameterized (Figures 4a–4c and 4m–4o).

In the subtropics and lower midlatitudes, the amount distribution problem exists, but is not as severe as in the tropics; in 50°S–15°S and 15°N–50°N, the amount mode is underestimated in CAM by a factor of 1.5–2 relative to SPCAM (Figures 4d–4f and 4j–4l). This is still a significant bias, but clearly the majority of the bias in the global amount distribution mode stems from the tropics. This latitudinal structure of the bias, high in the tropics and reduced at higher latitudes, suggests that the deficiency is associated with the convective parameterization, which produces the majority of rainfall in the tropics. The fractional contribution of

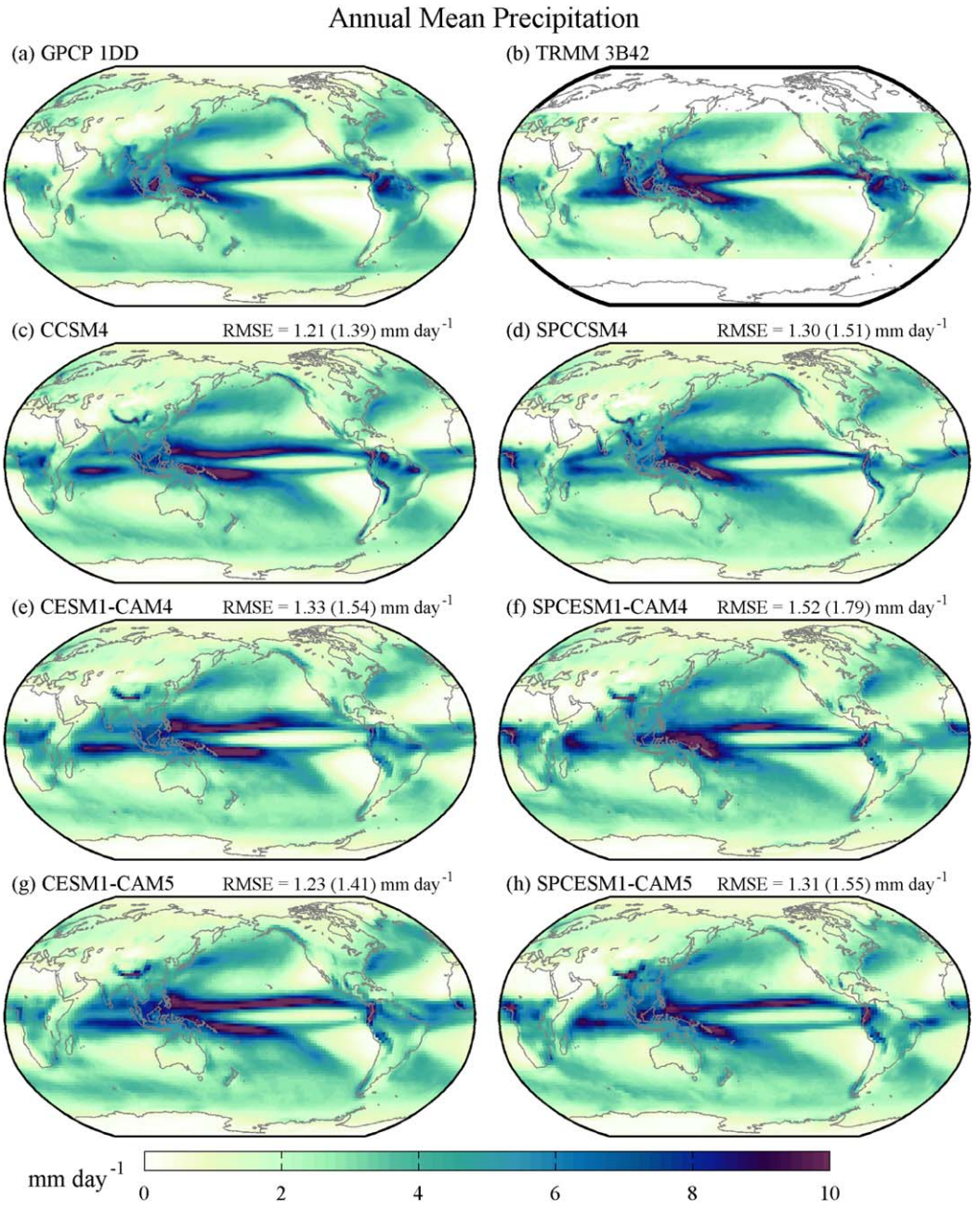

Figure 5. Annual mean precipitation (mm d^{-1}) from (a) GPCP 1DD, (b) TRMM 3B42, (c, d) (SP)CCSM4, (e, f) (SP)CESM1-CAM4, and (g, h) (SP)CESM1-CAM5 for (c, e, g) CAM and (d, f, h) SPCAM simulations; RMSE is relative to GPCP 1DD, and TRMM 3B42 in parentheses; GPCP 1DD, TRMM 3B42, and (SP)CCSM4 are shown at 1° resolution, and (SP)CESM1-CAM4 and (SP)CESM1-CAM5 are shown at 2° resolution.

resolved large-scale processes to total accumulated rainfall increases with latitude and produces the majority of rainfall poleward of 50°, where the bias is much lower.

Figures 2g–2i hone in on the tail of the frequency distribution, which captures the heaviest rainfall events. Again, there is a significant difference between observational estimates, with GPCP 1DD estimated percentile rates that are much weaker than TRMM 3B42. From this perspective, it appears that the conventionally parameterized CAM has the capacity to capture extreme storms that are as intense as TRMM 3B42 and SPCAM (Figure 2g), but as seen in *Yang et al*. [2014] the intensity is sensitive to horizontal resolution (Figures 2h and 2i). That is, in the coarse resolution configurations of CAM using CESM1-CAM4 and CESM1-CAM5

physics (Figures 2h and 2i) the 99.9th and 99.99th percentile rain rates (~50 and 75 mm d^{-1}) are about 75% as strong as in TRMM 3B42 (~75 and 120 mm d^{-1}). In contrast, in the finer-resolution configuration of CAM using CCSM4 physics (Figure 2g) the percentile rates are a good match to TRMM 3B42 and SPCAM. CAM's ability to match the observed intensity of the most extreme events appears to be very resolution dependent. However, this improvement in CAM's skill in capturing intense rain rates at higher resolution does not extend to more moderate rates, which are responsible for the twofold underestimation of the rainfall amount mode. Reassuringly, SPCAM produces a realistic scaling and intensity relative to TRMM 3B42 for extreme rainfall and the amount mode, in all versions analyzed, independent of horizontal resolution.

3.2. Mean Rainfall

Though there are substantial differences in the rainfall intensity distributions from GPCP 1DD and TRMM 3B42, their regional mean rainfall estimates (Table 1) and spatial patterns are very similar (Figures 5a and 5b). For instance, the spatial averages over the TRMM 3B42 region (50°S–50°N) are nearly the same with 2.89 ± 0.03 and 2.91 ± 0.03 mm d^{-1} for GPCP 1DD and TRMM 3B42, respectively (Table 1).

The models' time-mean rainfall, shown in Figures 5c–5h, reveals surprising similarities between conventional and superparameterization versions of CESM. All model versions produce a double-ITCZ rainfall bias, with too much rainfall off the equator throughout the Pacific extending to the East Pacific. However, the West Pacific bias (magnitude and Southeastward orientation of the SPCZ) is somewhat improved with superparameterization. All models also feature a zonal dipole rainfall bias in the Indian Ocean, with too much rainfall over the West and too little over the East Indian Ocean, as well as a dry bias over South America and the subtropical Atlantic Ocean. The Amazonian dry bias is amplified with superparameterization and extends into the East Pacific Ocean. This leads to somewhat higher root mean square errors in the geographic pattern of time mean rainfall than in the standard CAM, by 0.1–0.2 mm d^{-1}, depending on model version. SPCAM also tends to have slightly less rainfall than CAM in other regions, especially over land, but there is strong version dependence.

It is natural to wonder whether El Niño Southern Oscillation (ENSO) phase variability plays a role in the relatively short (10 year and 5 year) samples of ocean-coupled climate model integration analysis. We view this as unlikely to have been the case given the resilience of the time-mean rainfall bias pattern across model versions. This is confirmed in supporting information Figure S1, which shows that the essence of these bias patterns survives independent ENSO phase subcompositing based on the freely evolving internal ENSO in the (SP)CCSM4 simulations (following the ENSO precipitation index from *Curtis and Adler* [2000]). The double-ITCZ and off equatorial Pacific wet bias and Amazonian dry bias are all present in both the El Niño and La Niña ENSO phases for CAM and SPCAM.

The most striking finding of this analysis is that the mean rainfall bias pattern is relatively insensitive to superparameterization. This is somewhat inconsistent with the effects of superparameterization documented in an earlier coupled version of CCSM, in which adding explicit convection helped to improve time mean rainfall biases and reduce the double-ITCZ problem [*Stan et al*., 2010]. However, that study focused only on Winter and Summer seasonal patterns rather than annual mean, neglecting the Spring ITCZ transitional period, which contributes most to the annual double-ITCZ problem seen here in both models (not shown). Future work will expand our analysis to include a seasonal evaluation of rainfall and focus on regional processes such as the ITCZ transition as well as Asian and African monsoons. Though from this analysis it is evident that the effect of superparameterization on mean rainfall is model version dependent, and embedded explicit convection may not alone provide a cure to the double-ITCZ problem.

3.3. Dry Day Frequency

A key aspect of rainfall variability, invisible in the rainfall frequency distribution plots in section 3.1, is the dry day frequency—the occurrence of days producing accumulated rainfall less than 0.1 mm. Following the example of *Pendergrass and Hartmann* [2014b, 2014c], we include an analysis of this statistic that reflects the occurrence of rates below the lowest bin used for distribution analysis (Figure 6 and Table 2). We also evaluate the dry day frequency with a higher threshold (1.0 mm) in supporting information Figure S2 in order to assuage some of the known discrepancies between observations and models discussed above.

The main features of the dry day frequency geographic patterns represented in both observations and models (Figures 6a and 6b) include low frequency over tropical and midlatitude oceans (regions of high

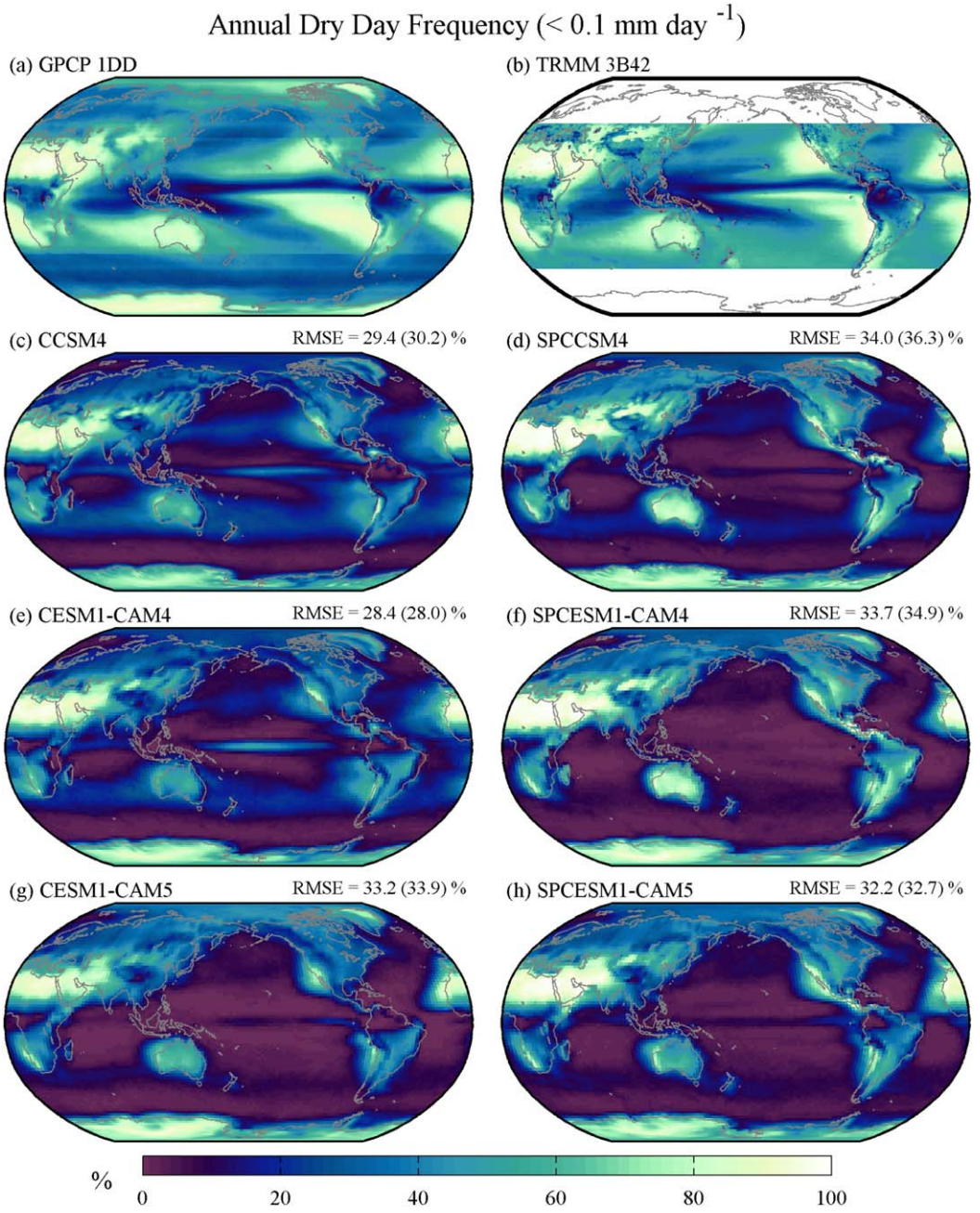

Figure 6. Annual dry day (<0.1 mm d^{-1}) frequency (%) from (a) GPCP 1DD, (b) TRMM 3B42, (c, d) (SP)CCSM4, (e, f) (SP)CESM1-CAM4, and (g, h) (SP)CESM1-CAM5 for (c, e, g) CAM and (d, f, h) SPCAM simulations; RMSE is relative to GPCP 1DD, and TRMM 3B42 in parentheses; GPCP 1DD, TRMM 3B42, and (SP)CCSM4 are shown at 1° resolution, and (SP)CESM1-CAM4 and (SP)CESM1-CAM5 are shown at 2° resolution.

time-mean rainfall), and higher frequency over subtropical oceans, especially subtropical stratocumulus regions off the western coast of most continents, and most landmasses. The two observational estimates are in fairly good agreement, especially given their uncertainty in remotely sensing very light drizzle. The most striking bias in all models is an apparent underestimate of dry day frequency over all oceans (more than 25%), most significantly in the subtropical Eastern Pacific (more than 50%), where very high frequencies are observed (or very light rain is not measured). This problem is reduced when the threshold is increased to 1.0 mm (supporting information Figure S2), where most of the model bias patterns in dry day frequency resemble the time-mean rainfall biases in Figure 5.

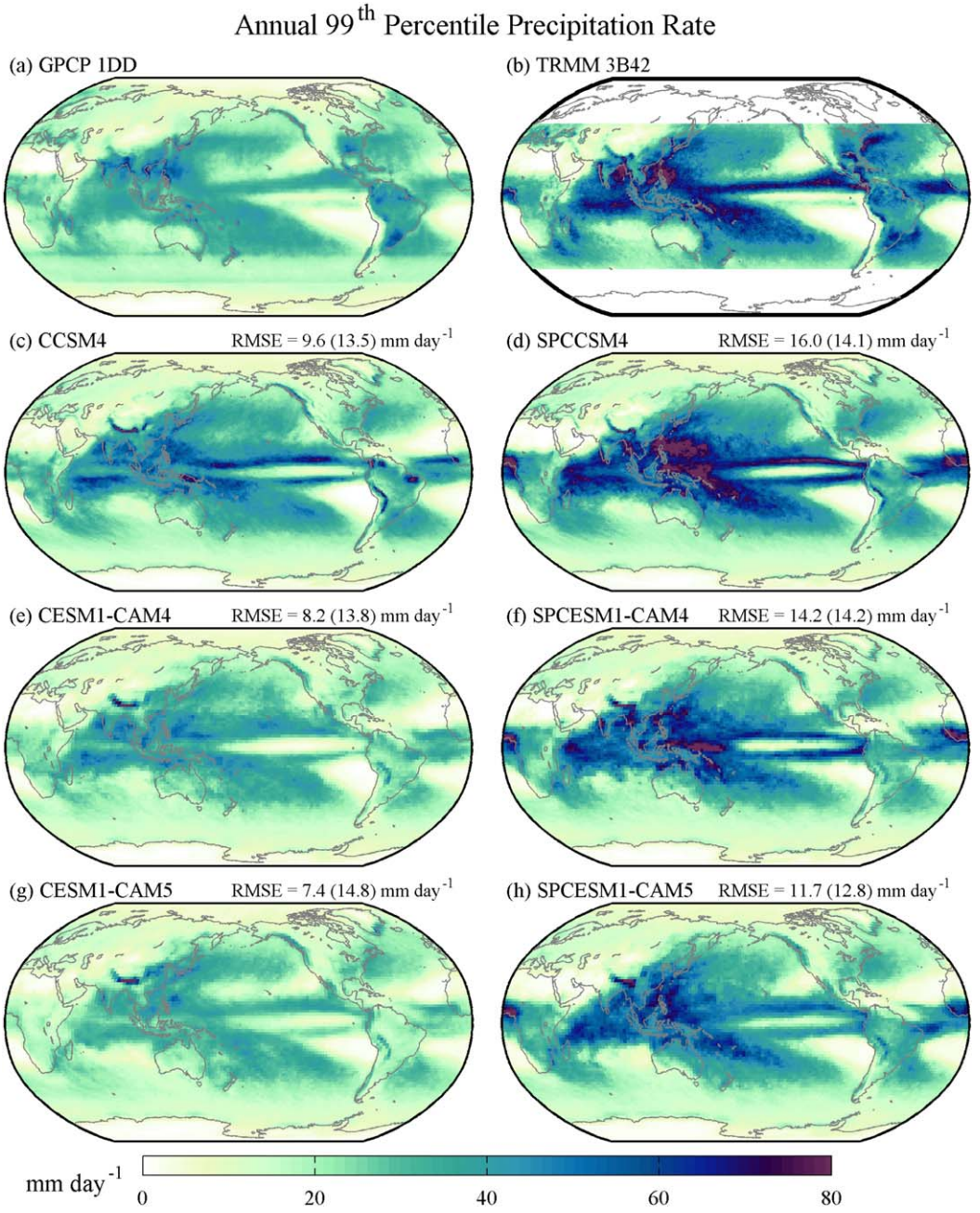

Figure 7. Annual 99th percentile rate (mm d^{-1}) from (a) GPCP 1DD, (b) TRMM 3B42, (c, d) (SP)CCSM4, (e, f) (SP)CESM1-CAM4, and (g, h) (SP)CESM1-CAM5 for (c, e, g) CAM and (d, f, h) SPCAM simulations; RMSE is relative to GPCP 1DD, and TRMM 3B42 in parentheses; GPCP 1DD, TRMM 3B42, and (SP)CCSM4 are shown at 1° resolution, and (SP)CESM1-CAM4 and (SP)CESM1-CAM5 are shown at 2° resolution.

Figure 6 shows that one especially interesting but hitherto unrealized effect of superparameterization is to increase the dry day frequency over land relative to conventionally parameterized CAM. In CAM, there are ∼20% fewer dry days than in the observations in many continental regions. In SPCAM, many regions have no bias or have up to ∼20% more dry days over land than observations. This is a robust effect of superparameterization across model versions. The higher frequency over land with superparameterization is balanced somewhat by lower dry day frequency over the ocean, or an increase in the occurrence of very light rain. Decreases in oceanic dry day frequency similar to the effects of superparameterization can also be seen in the transition to the latest version of conventionally parameterized CESM1 with CAM5 physics. This adds to the evidence that updates to low cloud physics in CAM5

Table 3. Annual 99th Percentile Precipitation Rate With 95% Confidence Interval (mm d^{-1})[a]

Region	GPCP 1DD	TRMM 3B42	CCSM4	SPCCSM4	CESM1 CAM4	SPCESM1 CAM4	CESM1 CAM5	SPCESM1 CAM5
90°S–90°N	22.6 ± 0.2		25.4 ± 0.4	29.8 ± 0.1	21.1 ± 0.3	26.8 ± 0.8	19.2 ± 0.5	25.1 ± 0.6
^{L}90°S–90°N	20.0 ± 0.3		20.7 ± 0.2	21.7 ± 0.2	17.0 ± 0.5	20.0 ± 0.9	15.5 ± 0.2	20.3 ± 0.4
^{O}90°S–90°N	23.7 ± 0.3		27.3 ± 0.5	33.2 ± 0.2	22.7 ± 0.4	29.5 ± 0.8	20.8 ± 0.6	27.1 ± 0.8
50°S–50°N	25.4 ± 0.2	34.3 ± 0.3	29.0 ± 0.5	34.8 ± 0.2	23.9 ± 0.4	31.4 ± 1.0	21.4 ± 0.6	29.0 ± 0.8
^{L}50°S–50° N	24.4 ± 0.4	27.0 ± 0.3	24.8 ± 0.3	26.1 ± 0.3	20.2 ± 0.7	24.3 ± 1.2	17.9 ± 0.5	24.7 ± 0.6
^{O}50°S–50°N	25.8 ± 0.3	36.9 ± 0.5	30.5 ± 0.6	37.9 ± 0.3	25.3 ± 0.5	33.9 ± 1.0	22.6 ± 0.7	30.5 ± 1.1
90°S–50°S	13.0 ± 0.4		12.5 ± 0.1	12.5 ± 0.1	11.1 ± 0.3	11.0 ± 0.3	11.3 ± 0.2	12.1 ± 0.4
50°S–15°S	24.3 ± 0.2	30.1 ± 0.7	25.8 ± 0.2	28.8 ± 0.3	21.8 ± 0.4	25.8 ± 1.0	20.3 ± 0.7	25.2 ± 0.4
15°S–15°N	28.4 ± 0.4	42.4 ± 0.5	36.8 ± 1.3	47.8 ± 0.6	29.0 ± 1.0	43.3 ± 1.7	24.3 ± 1.2	39.2 ± 1.6
15°N–50°N	23.5 ± 0.4	30.3 ± 0.5	24.2 ± 0.4	27.6 ± 0.2	20.8 ± 0.4	24.6 ± 0.6	19.5 ± 0.7	22.1 ± 1.0
50°N–90° N	14.0 ± 0.6		14.5 ± 0.1	14.5 ± 0.1	12.9 ± 0.1	13.3 ± 0.3	13.6 ± 0.2	13.9 ± 0.4

[a]Superscripts L and O denote land-only and ocean-only averaging regions, respectively.

parameterizations have led to a convergence with superparameterization results for oceanic drizzle variability.

In general, dry day frequency biases in SPCAM are very similar to their conventional CAM counterparts, but this analysis has revealed some interesting differences. There is a robust effect of superparameterization to produce more dry days over land, and the updated version of CESM1-CAM5 simulates more frequent drizzle over ocean as seen with superparameterization.

3.4. Extreme Rainfall Intensity

In section 3.1 we noted that superparameterization produces strong effects on heavy rain rates, especially in the tropics. Figure 7 hones in on the extreme rain by analyzing the 99th percentile rain rate in each model grid point to gain a geographic view. Average 99th percentile values over broad latitudinal regions are given in Table 3. And a complementary intensity metric, the total accumulated rainfall from rates above 50 mm d^{-1}, is presented in supporting information Figure S3.

The observational products (Figures 7a and 7b) disagree significantly about the magnitude of the 99th percentile rain rate, consistent with previous results demonstrating that TRMM 3B42 detects a larger right tail than the GPCP 1DD daily product. Because the two observations are so different, neither is appropriate for evaluating model biases, and we instead show the baseline simulations results in Figures 7c–7h. We have reasons to suspect that the heavier tail in TRMM 3B42 is the more plausible estimate, as discussed in section 2.1. This is supported by the fact that the higher-resolution version of CAM approaches the TRMM 3B42 estimate, and GPCP 1DD and TRMM 3B42 estimates are in good agreement over land where both products are more constrained by surface measurements. But we acknowledge that it is hard to define a true "bias" for statistics of the tail using these global gridded products, and focus our attention mostly on robust effects of superparameterization, which are interesting in their own right.

As expected from our analysis in section 3.1, the 99th percentile rain rates are systematically weaker in the conventionally parameterized CAM than in SPCAM. This is especially true when coarse resolution is used (Figures 7e and 7g), although even the elevated extreme rain rates of the finer resolution 1° CCSM4 simulation (Figure 7c) are weaker than those in TRMM 3B42 (Figure 7b) and SPCCSM4 at the same exterior resolution (Figure 7d). The extreme rainfall rates with superparameterization are not as sensitive to horizontal resolution (Figure 7d versus Figures 7f and 7h and Table 3) as they are with standard CAM (Figure 7c versus Figures 7e and 7g and Table 3), illustrating the potential for "scale-awareness" of superparameterization. A similar result is evident with the alternative intensity metric depicted in supporting information Figure S3, in which very little accumulated rainfall is produced by rates greater than 50 mm d^{-1} in the lower-resolution versions of CAM. The increased rainfall intensity in all versions SPCAM is in better agreement with the magnitude measured by TRMM 3B42 over its entire footprint (Table 3), with average values of 34.3 ± 0.3, 29.0 ± 0.5, 34.8 ± 0.2 mm d^{-1} for TRMM 3B42, CCSM4, and SPCCSM4, respectively. Though some regions are more intense than TRMM 3B42 in the 1° SPCCSM4 version.

Many of the distinct geographic patterns in the 99th percentile rate are linked to mean state rainfall patterns shared by both model classes, for instance over the East/Central Pacific and outside of the tropics and the Amazon region. This is unsurprising; it is logical that the tail of the precipitation distribution will scale to

a large extent with the mean of the distribution. This is also evident in the undersimulation of rainfall intensity in most of the Atlantic Ocean outside of the tropics seen in all model versions. In general, CAM and SPCAM simulate strikingly similar 99th percentile rain rates outside of the tropics, confirming the insensitivity of the rainfall distribution to superparameterization at higher latitudes noted earlier (section 3.1). For instance, the geographic pattern of extreme rainfall statistics in the storm tracks and over midlatitude continents are similarly captured in both SPCAM and CAM.

Of especial interest is the fact that in many tropical geographic action centers, superparameterization produces strong 99th percentile rain rates distinct from CAM that cannot be explained by difference in time mean rainfall. For instance, in the waters surrounding equatorial Africa (West Indian Ocean and Eastern equatorial Atlantic Ocean) all of the superparameterized versions of CAM simulate rainfall intensity far larger than standard CAM, and the TRMM 3B42 observations. These model differences in extremes occur despite all the model version pairs having similar magnitude mean rainfall biases in this region (Figure 5). Similarly, over the equatorial African continent CAM simulated a mean rainfall wet bias, but a rainfall intensity weaker than TRMM 3B42, while SPCAM has very little or no intensity bias in the region. These patterns indicate that part of the tropical rainfall distribution tail boost due to superparameterization may be linked to an enhanced African monsoon amplitude and stronger African Easterly Wave activity [*McCrary et al*., 2014]. Likewise, the Asian monsoon is one of the most prominent features of rainfall intensity in the TRMM 3B42 observations, which is captured in SPCAM [*DeMott et al*., 2011]. The geographic pattern of these monsoons is evident to some extent in the CAM simulations, but at a much weaker magnitude. Similar effects of superparameterization boosting extreme rainfall can be seen across the South Pacific Convergence Zone and the equatorial and tropical Western Pacific, suggesting another link to the Madden-Julian Oscillation, which is known to be stronger in SPCAM than CAM [*Benedict and Randall*, 2009].

In summary, the enhanced rainfall intensity with superparameterization is in better agreement with TRMM 3B42 observations than conventional CAM. With the exception of a few regions with strong wet mean state biases, conventional CAM significantly undersimulates 99th percentile rainfall intensity. Furthermore, the enhanced intensity in SPCAM is linked to geographic action centers reminiscent of African and Asian monsoons, African Easterly Waves, and the Madden-Julian Oscillation. An impact of superparameterization on extreme rainfall rates is difficult to detect outside of the tropics, and the two model formulations begin to converge through the extra-tropics and into higher latitudes. This result suggests that large-scale processes in CAM, which play a larger role at high latitudes, are capable of producing realistic rain rates, while the convective parameterizations produce rates that are too weak across the rainfall spectrum.

3.5. Rainfall Amount Mode

We have argued that the mode of the rainfall amount distribution—reflecting the rain rate that delivers the most accumulated rainfall—is an important physical diagnostic that seems to reveal especially striking effects of superparameterization. Figure 8 examines the geographic pattern of the amount mode calculated for each grid point independently. This diagnostic has not been highlighted in previous climate model evaluation, but we find it especially revealing.

One issue is that the mode of the distribution can be difficult to estimate at the grid point level because it requires a fit from the rainfall amount distribution, which depends on discrete rain rate bin spacing. The bins can be under-sampled in some areas, especially regions with little rain, even with 10 years of data, and can thus produce a noisy distribution at the grid point level. To alleviate this issue we apply light local horizontal smoothing, where the values shown in Figure 8 reflect the mode fit to a distribution that is a weighted average with neighboring grid points. We also analyze the mode over broad latitudinal averaged regions (Table 4) and compare to a complementary metric, the median, which is calculated independently from the distribution and does not require smoothing (supporting information Figure S4), but tells essentially the same story as the mode. We prefer to analyze the mode despite the methodological challenges in estimating it due to its special physical meaning, but have tested that the key findings from this analysis are supported by the median and broad regional averages.

Figures 8a and 8b show the geographic pattern of the amount mode in the data products, illustrating the level of disagreement in observational estimates. As with the 99th percentile rates, there is major observational uncertainty using the GPCP 1DD and TRMM 3B42 daily rainfall products for quantitative estimates of the amount mode. As a result, we analyze the baseline simulation results rather than the

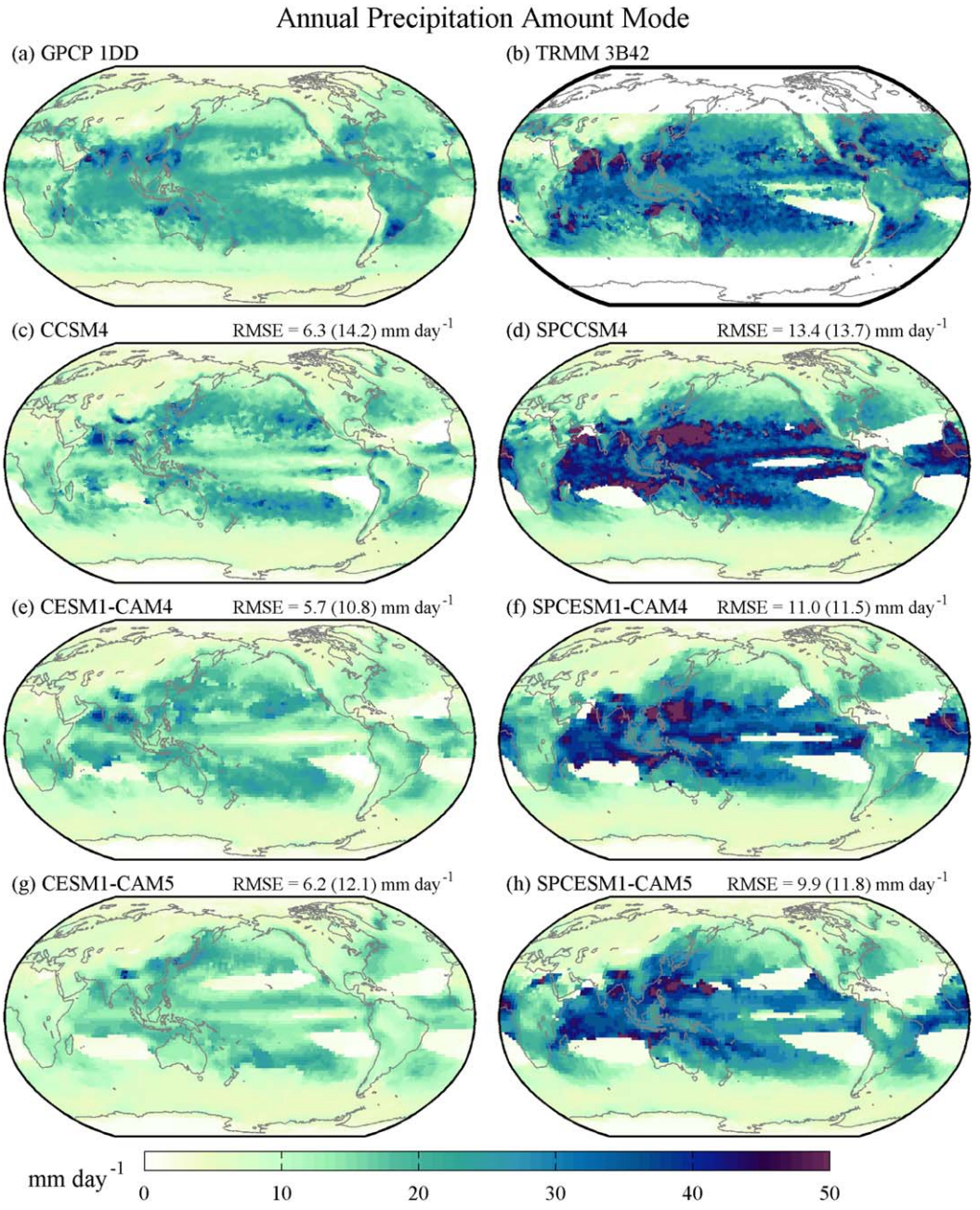

Figure 8. Annual amount mode (mm d^{-1}) from (a) GPCP 1DD, (b) TRMM 3B42, (c, d) (SP)CCSM4, (e, f) (SP)CESM1-CAM4, and (g, h) (SP)CESM1-CAM5 for (c, e, g) CAM and (d, f, h) SPCAM simulations; RMSE is relative to GPCP 1DD, and TRMM 3B42 in parentheses; GPCP 1DD, TRMM 3B42, and (SP)CCSM4 are shown at 1° resolution, and (SP)CESM1-CAM4 and (SP)CESM1-CAM5 are shown at 2° resolution.

bias in Figures 8c–8h. It is more surprising that there are discrepancies in the observed amount mode than it was for dry day frequency and extreme rainfall rates because light rain (less than 0.1 mm d^{-1}) and infrequent heavy rain is understandably difficult to remotely observe from space. However, the amount mode represents the rain rate that produces the most amount of rain and is in the range of rates that one might expect to be more easily observed. The largest differences between observational estimates of the amount mode occur over the ocean; the quantity is in better agreement over land (18.0 and 19.9 mm d^{-1} over land versus 19.9 and 29.1 mm d^{-1} over oceans for GPCP 1DD and TRMM 3B42, respectively, in the TRMM 3B42 footprint region, Table 4) where the products are more constrained by surface observations.

Table 4. Annual Precipitation Amount Mode With 95% Confidence Interval (mm d^{-1})[a]

Region	GPCP 1DD	TRMM 3B42	CCSM4	SPCCSM4	CESM1 CAM4	SPCESM1 CAM4	CESM1 CAM5	SPCESM1 CAM5
90°S–90°N	16.4 ± 0.6		12.3 ± 0.4	21.8 ± 1.5	12.3 ± 1.4	21.8 ± 2.6	12.3 ± 0.7	18.0 ± 2.8
^{L}90°S–90° N	16.4 ± 0.7		12.3 ± 0.6	18.0 ± 0.9	12.3 ± 0.8	16.4 ± 1.0	10.2 ± 0.9	18.0 ± 2.3
^{O}90°S–90° N	16.4 ± 0.6		12.3 ± 0.4	29.1 ± 1.6	14.9 ± 1.4	26.4 ± 2.2	14.9 ± 0.9	26.4 ± 3.9
50°S–50°N	18.0 ± 0.6	26.4 ± 1.2	14.9 ± 0.5	26.4 ± 1.0	14.9 ± 0.0	21.8 ± 2.5	13.6 ± 1.1	26.4 ± 2.8
^{L}50°S–50° N	18.0 ± 0.6	19.9 ± 0.8	13.6 ± 0.6	19.9 ± 0.9	13.6 ± 0.9	16.4 ± 2.3	11.2 ± 0.6	19.9 ± 3.6
^{O}50°S–50° N	19.9 ± 0.7	29.1 ± 1.3	14.9 ± 0.4	32.0 ± 1.2	14.9 ± 0.0	29.1 ± 3.1	14.9 ± 0.8	26.4 ± 1.8
90°S–50°S	8.4 ± 0.5		5.8 ± 0.2	5.8 ± 0.2	5.2 ± 0.7	5.2 ± 0.5	5.2 ± 0.3	5.8 ± 0.3
50°S–15°S	16.4 ± 0.5	24.0 ± 1.1	14.9 ± 0.8	16.4 ± 1.2	14.9 ± 1.4	13.6 ± 1.9	12.3 ± 0.7	18.0 ± 1.9
15°S–15°N	19.9 ± 0.7	29.1 ± 1.0	13.6 ± 0.5	38.7 ± 1.6	14.9 ± 0.0	32.0 ± 3.2	14.9 ± 0.8	26.4 ± 1.8
15°N–50° N	18.0 ± 0.7	24.0 ± 2.1	14.9 ± 1.4	19.9 ± 1.2	14.9 ± 1.4	21.8 ± 3.1	13.6 ± 1.1	18.0 ± 1.8
50°N–90° N	9.3 ± 0.5		7.7 ± 0.5	7.7 ± 0.4	6.3 ± 1.1	7.7 ± 0.8	7.7 ± 0.9	7.7 ± 1.1

[a]Superscripts L and O denote land-only and ocean-only averaging regions, respectively.

Again, we nominally assume the TRMM 3B42 observations (Figure 8b) provide a more meaningful estimate of rain rate intensity for reasons described previously. TRMM 3B42 highlights four distinct geographic action centers of highest amount mode (greater than 40 mm d^{-1}) in the Arabian Sea, the Bay of Bengal, the South China Sea, and off the coast of Northwestern Australia, regions associated with intense monsoonal rainfall variations. These regions are also the dominant features in the amount median (supporting information Figure S4), which also shows elevated values associated with the African monsoon and over warm waters of western boundary currents. The mode of TRMM 3B42's amount distribution is also greater than 25 mm d^{-1} across much of the tropical and subtropical oceans.

Reassuringly, SPCAM produces the geographic pattern of amount mode with similar magnitude to TRMM 3B42, greater than 25 mm d^{-1} in most tropical ocean regions and exceeding 50 mm d^{-1} in the same geographic action centers (Figures 8d, 8f, and 8h). SPCAM also highlights an action center off the west coast of Africa that is evident but weaker in TRMM 3B42—consistent with excessive modulation of submonthly rainfall extremes by an overactive African monsoon. SPCAM's amount mode is also in good agreement with both TRMM 3B42 and GPCP 1DD over land, as noted in Section 3.1. However, Figure 8 also reveals some important geographic biases in the amount mode magnitude in SPCAM. Most notably is the anomalously elevated and broad amount mode pattern in the northwestern tropical Pacific, a region where excessive time-mean rainfall has been documented in earlier uncoupled version SPCAM3.0 [*Khairoutdinov et al.*, 2005]. Although a time-mean rainfall bias in this region is not as striking in newer versions of SPCAM (Figure 5), it is interesting that the amount mode highlights the same geographic region as an ongoing area of model bias, systematically across superparameterized versions of ocean-coupled SPCAM.

More problematic is the systematically low amount mode magnitude in all versions of the conventionally parameterized CAM compared to both the SPCAM and TRMM 3B42 data. The spatial pattern in CAM does highlight a few action centers in the Indian Ocean, but is otherwise a reflection of the storm track patterns in the midlatitude Pacific that are poleward of high amount mode values in observations. In the storm track regions in CAM, large-scale precipitation plays a bigger role than parameterized convection, the likely source of the improvement in the region. The monsoon action centers in the Indian Ocean are much weaker in CAM relative to TRMM 3B42 and SPCAM, and CAM maintains mean monsoon rainfall by increasing daily rain frequency in the region rather than capturing the intensity (not shown). Unlike the 99th percentile rain rate, the problem with the amount mode does not improve with increased resolution in CAM (Figure 8c versus Figures 8e and 8g), suggesting it is fundamental to the deep convection parameterizations and not a limitation of resolution alone.

Comparing all SPCAM versions to their standard CAM counterparts, the most striking effects of superparameterization on the amount mode (Figures 8d, 8f, and 8h versus Figures 8c, 8e, and 8g) highlight an interesting and suggestive geographic structure. The patterns emphasize two off-equatorial action centers in the Indian and West Pacific tropical oceans, and on-equatorial action center east of the Maritime Continent and west of the Sahara. These geographic signatures tend to implicate monsoons and their connection to specific equatorial wave classes such as the Madden-Julian Oscillation, equatorial Rossby waves, and African Easterly Waves in driving the more realistically elevated tropical amount mode that results from superparameterization.

Differences in the modulation of submonthly rainfall intensity associated with the monsoon contribute significantly to the above effects. Off-line analysis of changes in daily rainfall variance approaching the month of peak monsoonal rainfall suggests that for the East Asian monsoon, SPCAM and CAM both produce monthly mean monsoon rainfall amplitudes of similar and realistic magnitude, but in SPCAM the monsoon more strongly modulates daily variance, in better agreement with TRMM 3B42 observations. In contrast, for the African monsoon SPCAM suffers from an excessive high bias in monthly mean amplitude and thus also overdoes its modulation of submonthly rainfall extremes across all versions. In contrast, CAM produces a more realistic monthly mean African monsoon amplitude but underestimates its modulation of submonthly rainfall. These differences in monsoon representation and the effects of monsoons on rainfall are important to understanding many model differences in tropical geographic action centers of amount mode and 99th percentile rainfall. A general effect of superparameterization appears to be boosting the effect of monsoons on daily rainfall intensity; in contrast CAM appears to sustain its mean monsoon amplitude primarily through variations in submonthly rainfall frequency.

4. Conclusions

In this study we target several features of accumulated daily rainfall that are fundamental to the hydrological cycle and therefore critical to society. However, many of these features are difficult to observe on global scales and poorly represented in GCMs making future climate change projections uncertain. We take the view that it is important to evaluate simulated rainfall in global climate models in depth by focusing on rainfall intensity distributions and extreme rates in addition to time-mean rainfall biases. Our analysis focuses on statistics from frequency and amount distributions, comparing rainfall simulated by three conventional and superparameterized versions of CAM against two gridded observational rainfall products, GPCP 1DD and TRMM 3B42.

Rainfall distributions demonstrate that superparameterization produces more realistic (relative to TRMM 3B42) elevated intensity for extreme rainfall and the amount mode, in all versions analyzed, independent of horizontal resolution. Conventionally parameterized CAM is sensitive to model version and resolution, with the higher resolution (1°) CCSM4 version able to capture some of the extreme rainfall intensity of the TRMM 3B42 and SPCAM highest percentile rates. Both CAM and SPCAM simulate more oceanic drizzle than is detectable by gridded rainfall products, but only the three SPCAM versions and the most modern version of CAM (CESM1-CAM5) capture a distinct drizzle peak mode in the frequency distribution.

The amount modes from TRMM 3B42 and GPCP 1DD are in good agreement over land, but the TRMM 3B42 product has systematically more intense rainfall over the ocean. SPCAM's amount mode matches both of these observations over land and is a better match to TRMM 3B42 over the ocean, but CAM's is systematically weaker than both observations regardless of resolution and version. The weak amount mode bias in CAM encapsulates ongoing problems with its deep convective parameterizations, and is dominated by the tropics where the convective parameterization contributes the most accumulated rainfall.

The geographic patterns of the amount mode and 99th percentile rates highlight the effects on extreme rainfall associated with important modes of tropical internal variability that are known to be impacted by cloud superparameterization. We have argued that spatial decomposition of these and other (mean rainfall and dry day frequency) diagnostics can help expose the regions that contribute most significantly to biases in area-mean rainfall distributions and helps diagnose underlying mechanisms leading to the improvements that can occur with superparameterization.

Mean rainfall biases are remarkably insensitive to superparameterization. All six model versions analyzed exhibit a double-ITCZ that extends into the East Pacific and too much off equatorial rainfall; features that are evident in both phases of internal ENSO variability. Regionally there are some differences in the magnitude of the bias; i.e., the West Pacific Southern Hemisphere double-ITCZ is somewhat improved with superparameterization, but the Amazonian dry bias is worse. Signals of double-ITCZ biases in the Indian Ocean also tend to be ameliorated by superparameterization across model versions.

Dry day frequency estimates from GPCP 1DD and TRMM 3B42 are in relatively good agreement and indicate similar magnitude biases for CAM and SPCAM. Either both models underestimate dry day frequency over oceans or there is a systematic underestimation of rainy days in the gridded observations that are unable to

measure very light rain. The bias is reduced with a higher threshold for dry day frequency and mostly resembles the mean state biases. In general, the frequency is increased over land as a result of superparameterization. Low biases (fewer dry days) are evident over oceans and land in CAM, but in SPCAM, negative biases are smaller or positive (more dry days) over land compared to observations. Updated low cloud physics in CESM1-CAM5 simulates more frequent light drizzle events over the ocean and more closely resembles the superparameterized dry day frequency result.

Extreme rainfall intensity becomes less sensitive to horizontal resolution and stronger, especially in regions of tropical wave activity, as a result of superparameterization. We measure rainfall intensity using two metrics—the 99th percentile rates and the accumulated rainfall from rates greater than 50 mm d^{-1}. For both metrics TRMM 3B42 and GPCP 1DD provide very different estimates of truth, with TRMM 3B42 containing more intense rainfall events. The low-resolution (2°) versions of conventionally parameterized CAM produce weaker intensity than TRMM 3B42 and SPCAM, and are similar to GPCP 1DD, but the high-resolution version (1° CCSM4) is able to capture some regional features observed by TRMM 3B42. Over broad regional analysis SPCAM is in good agreement with TRMM 3B42 observations and is insensitive to exterior resolution or model version for both metrics.

For the most part, intensity biases co-locate geographically with mean state biases, but there are some important regional exceptions: SPCAM produces higher intensity rainfall extremes in the equatorial oceans surrounding Africa despite reduced mean rainfall there, and CAM simulates reduced extremes over continental Africa despite a mean wet bias there. The changes in extreme rainfall intensity resulting from superparameterization highlight geographic regions suggesting they are related to increased tropical variability relative to CAM, with the most intense rates occurring in regions coincident with the Asian and African monsoons, African Easterly Waves, and the Madden-Julian Oscillation activity centers. Outside of the tropics (e.g., storm tracks) CAM and SPCAM intensities are more similar, likely due to an increased contribution from resolved-scale rainfall in CAM.

Rainfall amount mode is favorably boosted and concentrated in geographic regions of tropical waves and monsoons as a result of cloud superparameterization. The rainfall amount mode is an important physical quantity; it represents the rain rate that delivers the most accumulated surface reaching rainfall. GPCP 1DD and TRMM 3B42 agree on some aspects of the amount mode spatial pattern, but consistent with weaker intensity, the magnitude is lower in GPCP 1DD. TRMM 3B42 and SPCAM, and to some extent GPCP 1DD, identify four distinct geographic action centers of high amount mode in the Arabian Sea, the Bay of Bengal, the South China Sea, and off the coast of Northwestern Australia. The geographic action centers where the amount mode responds most to superparameterization highlight two off-equatorial regions in the Indian and West Pacific Oceans, and an on-equatorial region east of the Maritime Continent that again suggest links to tropical waves, monsoons, and the Madden-Julian Oscillation. In these regions, SPCAM's amount mode is more intense than TRMM 3B42, especially the northwestern tropical Pacific, indicating an ongoing problem in this region, which has a time-mean wet rainfall bias in earlier coupled versions of SPCAM. An increase in the monsoon modulation of submonthly rainfall extremes appears to play an especially important role. Overall superparameterization appears to improve the amount mode relative to CAM, which is much lower than TRMM 3B42 in all versions, and exhibits unrealistically weak geographic variability. Additionally, the amount mode in CAM does not improve with higher resolution, unlike extreme rain, indicating a fundamental problem with convective parameterization.

Overall, this study has highlighted important differences in the character of rainfall simulated with conventional and superparameterized GCMs, enabled by analyzing multiple model versions and configurations of CAM and SPCAM. It has revealed where we might expect to trust the simulated sensitivities of rainfall and where we should be suspicious. With this context, forthcoming work will analyze climate change experiments investigating the response of the rainfall distributions and metrics evaluated here in identical CAM-SPCAM version pairs to higher CO_2 concentrations. Additional work is ongoing to decompose the contributions of convective versus large-scale rainfall in CAM to the total distribution, and determine which portions of the rainfall spectrum these processes (parameterizations) control, to better understand the nature of the amount mode bias under conventional parameterization. We are also working to unfold the connection between tropical wave activity and rainfall intensity geographic action centers to better understand the mechanistic relationship, evaluate its realism against observations, and develop a framework for expected regional changes and implications due to climate forcing.

Acknowledgments

Kooperman acknowledges funding for this work from an NSF Postdoctoral Research Fellowship (AGS-1349579). Pritchard acknowledges funding from the NSF (AGS-1419518) and DOE (DE-SC0012152 and DE-SC0012548). CESM development is led by NCAR and supported by the NSF and DOE; NCAR is sponsored by the NSF. Development of superparameterization is led by CMMAP, funded by the NSF (ATM-0425247) and managed by Colorado State University. CCSM4 simulations were run at the DOE National Center for Computational Sciences at Oak Ridge National Laboratory (DE-AC05-00OR22725). SPCCSM4 simulations were run at the DOE National Energy Research Scientific Computing Center (DE-AC02-05CH11231) and supported by the Regional and Global Climate Modeling Program (SC0006722). (SP)CESM1-CAM4 and (SP)CESM1-CAM5 simulations were run at the NSF NCAR Computational and Information Systems Laboratory on Yellowstone (UCIR0012 and UCSU0006). SPCCSM4 and CCSM4 output is available on the Earth System Grid (www.earthsystemgrid.org). (SP)CESM1-CAM4 and (SP)CESM1-CAM5 output is available on request from mark@atmos.colostate.edu and mburt@atmos.colostate.edu, respectively. GPCP 1DD and TRMM TMPA 3B42 data were provided by the NASA GSFC Mesoscale Atmospheric Processes Laboratory, which develops 1DD as a contribution to the GEWEX Global Precipitation Climatology Project and TMPA 3B42 as a contribution to TRMM. GPCP 1DD and TRMM 3B42 data are available from NASA GSFC RSD (ftp://rsd.gsfc.nasa.gov/pub/1dd-v1.2/) and Mirador (http://mirador.gsfc.nasa.gov), respectively. The authors are grateful to Cristiana Stan and Li Xu for providing SPCCSM4 output. The authors also thank the reviewers for insightful comments and suggestions.

References

Alemohammad, S. H., K. A. McColl, A. G. Konings, D. Entekhabi, and A. Stoffelen (2015), Characterization of precipitation product errors across the United States using multiplicative triple collocation, *Hydrol. Earth Syst. Sci.*, *19*, 3489–3503.

Allan, R. P., C. Liu, M. Zahn, D. A. Lavers, E. Koukouvagias, and A. Bodas-Salcedo (2014), Physically consistent responses of the global atmospheric hydrological cycle in models and observations, *Surv. Geophys.*, *35*, 533–552.

Allen, M. R., and W. J. Ingram (2002), Constraints on future changes in climate and the hydrologic cycle, *Nature*, *419*, 224–232.

Arakawa, A., and W. H. Schubert (1974), Interaction of a cumulus cloud ensemble with the large-scale environment, Part I, *J. Atmos. Sci.*, *31*, 674–701.

Behrangi, A., M. Lebsock, S. Wong, and B. Lambrigtsen (2012), On the quantification of oceanic rainfall using spaceborne sensors, *J. Geophys. Res.*, *117*, D20105, doi:10.1029/2012JD017979.

Benedict, J. J., and D. A. Randall (2009), Structure of the Madden-Julian oscillation in the superparameterized CAM, *J. Atmos. Sci.*, *66*(11), 3277–3296.

Bretherton, C. S., and S. Park (2009), A new moist turbulence parameterization in the Community Atmosphere Model, *J. Clim.*, *22*, 3422–3448.

Campin, J.-M., C. Hill, H. Jones, and J. Marshall (2011), Super-parameterization in ocean modeling: Application to deep convection, *Ocean Modell.*, *36*, 90–101.

Cavanaugh, N. R., A. Gershunov, A. K. Panorska, and T. J. Kozubowski (2015), The probability distribution of intense daily precipitation, *Geophys. Res. Lett.*, *42*, 1560–1567, doi:10.1002/2015GL063238.

Chou, C., C.-A. Chen, P.-H. Tan, and K. T. Chen (2012), Mechanisms for global warming impacts on precipitation frequency and intensity, *J. Clim.*, *25*(9), 3291–3306.

Curtis, S., and R. Adler (2000), ENSO indices based on patterns of satellite-derived precipitation, *J. Clim.*, *13*, 2786–2793.

Dai, A. (2006), Precipitation characteristics in eighteen coupled climate models, *J. Clim.*, *19*, 4605–4630.

DeMott, C. A., D. A. Randall, and M. Khairoutdinov (2007), Convective precipitation variability as a tool for general circulation model analysis, *J. Clim.*, *20*, 91–112.

DeMott, C. A., C. Stan, D. A. Randall, J. L. Kinter III, and M. Khairoutdinov (2011), The Asian monsoon in the superparameterized CCSM and its relationship to tropical wave activity, *J. Clim.*, *24*, 5134–5156.

Dinku, T., P. Ceccato, and S. J. Connor (2011), Challenges of satellite rainfall estimation over mountainous and arid parts of east Africa, *Int. J. Remote Sens.*, *30*, 5965–5979.

Dirmeyer, P. A., C. A. Schlosser, and K. L. Brubaker (2009), Precipitation, recycling, and land memory: An integrated analysis, *J. Hydrometeorol.*, *10*, 278–288.

Gent, P. R., et al. (2011), The Community Climate System Model version 4, *J. Clim.*, *24*, 4973–4991.

Grabowski, W. W. (2001), Coupling cloud processes with the large-scale dynamics using the cloud-resolving convection parameterization (CRCP), *J. Atmos. Sci.*, *58*(9), 978–997.

Gustafson, W. I., Jr., L. K. Berg, R. C. Easter, and S. J. Ghan (2008), The explicit-cloud parameterized-pollutant hybrid approach for aerosol-cloud interactions in multiscale modeling framework models: Tracer transport results, *Environ. Res. Lett.*, *3*, 1–7.

Gustafson, W. I., Jr., P.-L. Ma, and B. Singh (2014), Precipitation characteristics of CAM5 physics at mesoscale resolution during MC3E and the impact of convective timescale choice, *J. Adv. Model. Earth Syst.*, *6*, 1271–1287, doi:10.1002/2014MS000334.

Held, I. M., and B. J. Soden (2006), Robust responses of the hydrological cycle to global warming, *J. Clim.*, *19*, 5686–5699.

Hennessy, K. J., J. M. Gregory, and J. F. B. Mitchell (1997), Changes in daily precipitation under enhanced greenhouse conditions, *Clim. Dyn.*, *13*, 667–680.

Huffman, G. J., et al. (1997), The global precipitation climatology project (GPCP) combined precipitation dataset, *Bull. Am. Meteorol. Soc.*, *78*, 5–20.

Huffman, G. J., R. F. Adler, M. M. Morrissey, S. Curtis, R. Joyce, B. McGavock, and J. Susskind (2001), Global precipitation at one-degree daily resolution from multi-satellite observations, *J. Hydrometeorol.*, *2*, 36–50.

Huffman, G. J., D. T. Bolvin, E. J. Nelkin, D. B. Wolff, R. F. Adler, G. Gu, Y. Hong, K. P. Bowman, and E. F. Stocker (2007), The TRMM multisatellite precipitation analysis (TMPA): Quasi-global, multiyear, combined-sensor precipitation estimates at fine scales, *J. Hydrometeorol.*, *8*, 38–55.

Huffman, G. J., D. T. Bolvin, and R. F. Adler (2012a), GPCP Version 1.2 1-Degree Daily (1DD) Precipitation Data Set, World Data Center A, National Climatic Data Center, Asheville, N. C. [Available at ftp://rsd.gsfc.nasa.gov/pub/1dd-v1.2/.]

Huffman, G. J., E. F. Stocker, D. T. Bolvin, E. J. Nelkin, and R. F. Adler (2012b), TRMM Version 7 3B42 and 3B43 Data Sets, National Aeronautics and Space Administration/Goddard Space Flight Center, Greenbelt, Md. [Available at http://mirador.gsfc.nasa.gov.]

Hunke, E. C., and W. H. Lipscomb (2008), CICE: The Los Alamos sea ice model user's manual, version 4, *Tech. Rep. LA-CC-06-012*, 76 pp., Los Alamos Natl. Lab., Los Alamos, NM.

Iacono, M. J., J. S. Delamere, E. J. Mlawer, M. W. Shephard, S. A. Clough, and W. D. Collins (2008), Radiative forcing by long-lived greenhouse gases: Calculations with the AER radiative transfer models, *J. Geophys. Res.*, *113*, D13103, doi:10.1029/2008JD009944.

Jones, C. R., C. S. Bretherton, and M. S. Pritchard (2015), Mean state acceleration of cloud resolving models and large eddy simulations, *J. Adv. Model. Earth Syst.*, *7*, 1–18, doi:10.1002/2015MS000488.

Khairoutdinov, M., D. Randall, and C. DeMott (2005), Simulations of the atmospheric general circulation using a cloud-resolving model as a superparameterization of physical processes, *J. Atmos. Sci.*, *62*(7), 2136–2154.

Khairoutdinov, M. F., and D. A. Randall (2001), A cloud resolving model as a cloud parameterization in the NCAR Community Climate System Model: Preliminary results, *Geophys. Res. Lett.*, *28*(18), 3617–3620.

Khairoutdinov, M. F., and D. A. Randall (2003), Cloud resolving modeling of the ARM summer 1997 IOP: Model formulation, results, uncertainties, and sensitivities, *J. Atmos. Sci.*, *60*, 607–625.

Kooperman, G. J., M. S. Pritchard, and R. C. J. Somerville (2013), Robustness and sensitivities of Central U.S. summer convection in the super-parameterized CAM: Multi-model intercomparison with a new regional EOF index, *Geophys. Res. Lett.*, *40*, 3287–3291, doi:10.1002/grl.50597.

Kooperman, G. J., M. S. Pritchard, and R. C. J. Somerville (2014), The response of US summer rainfall to quadrupled CO_2 climate change in conventional and super-parameterized versions of the NCAR Community Atmosphere Model, *J. Adv. Model. Earth Syst.*, *6*, 859–882, doi:10.1002/2014MS000306.

Kopparla, P., E. M. Fischer, C. Hannay, and R. Knutti (2013), Improved simulation of extreme precipitation in a high-resolution atmosphere model, *Geophys. Res. Lett.*, *40*, 5803–5808, doi:10.1002/2013GL057866.

Koster, R. D., et al. (2004), Regions of strong coupling between soil moisture and precipitation, *Science*, *305*(5687), 1138–1140.
Lawrence, D. M., et al. (2011), Parameterization improvements and functional and structural advances in version 4 of the Community Land Model, *J. Adv. Model. Earth Syst.*, *3*, M03001, doi:10.1029/2011MS000045.
Li, F., D. Rosa, W. D. Collins, and M. F. Wehner (2012), "Super-parameterization": A better way to simulate regional extreme precipitation?, *J. Adv. Model. Earth Syst.*, *4*, M04002, doi:10.1029/2011MS000106.
Liu, C., and R. P. Allan (2012), Multi-satellite observed responses of precipitation and its extremes to interannual climate variability, *J. Geophys. Res.*, *117*, D03101, doi:10.1029/2011JD016568.
Liu, X., et al. (2012), Toward a minimal representation of aerosols in climate models: Description and evaluation in the Community Atmosphere Model CAM5, *Geosci. Model Dev.*, *5*(3), 709–739.
Mahlstein, I., R. W. Portmann, J. S. Daniel, S. Solomon, and R. Knutti (2012), Perceptible changes in regional precipitation in a future climate, *Geophys. Res. Lett.*, *39*, L05701, doi:10.1029/2011GL050738.
Marchand, R., and T. T. Ackerman (2010), An analysis of cloud cover in multiscale modeling framework global climate model simulations using 4 and 1 km horizontal grids, *J. Geophys. Res.*, *115*, D16207, doi:10.1029/2009JD013423.
McCrary, R. R., D. A. Randall, and C. Stan (2014), Simulations of the West African monsoon with a superparameterized climate model. Part II: African easterly waves, *J. Clim.*, *27*, 8323–8341.
Morrison, H., and A. Gettelman (2008), A new two-moment bulk stratiform cloud microphysics scheme in the Community Atmosphere Model, version 3 (CAM3). Part I: Description and numerical tests, *J. Clim.*, *21*(15), 3642–3659.
Morrison, H., J. A. Curry, and V. I. Khvorostyanov (2005), A new double-moment microphysics parameterization for application in cloud and climate models. Part I: Description, *J. Atmos. Sci.*, *62*(6), 1665–1677.
Neale, R. B., et al. (2010a), *Description of the NCAR Community Atmosphere Model (CAM 4.0)*, NCAR Technical Note: NCAR/TN-485+STR, Natl. Cent. for Atmos. Res., Boulder, Colo.
Neale, R. B., et al. (2010b), *Description of the NCAR Community Atmosphere Model (CAM 5.0)*, NCAR Technical Note: NCAR/TN-486+STR, Natl. Cent. for Atmos. Res., Boulder, Colo.
O'Gorman, P. A. (2012), Sensitivity of tropical precipitation extremes to climate change, *Nat. Geosci.*, *5*, 697–700.
O'Gorman, P. A. (2015), Precipitation extremes under climate change, *Curr. Clim. Change Rep.*, *1*, 49–59.
O'Gorman, P. A., and T. Schneider (2009), The physical basis for increases in precipitation extremes in simulations of 21st-century climate change, *Proc. Natl. Acad. Sci. U. S. A.*, *106*(35), 14,773–14,777.
Panorska, A. K., A. Gershunov, and T. J. Kozubowski (2007), From diversity to volatility: Probability of daily precipitation extremes, in *Nonlinear Dynamics in Geophysics*, edited by A. A. Tsonis and J. B. Elsner, pp. 465–484, Springer, N. Y.
Park, S., and C. S. Bretherton (2009), The University of Washington shallow convection and moist turbulence schemes and their impact on climate simulations with the Community Atmosphere Model, *J. Clim.*, *22*(12), 3449–3469.
Peel, M. C., B. L. Finlayson, and T. A. McMahon (2007), Updated world map of the Koppen-Geiger climate classification, *Hydrol. Earth Syst. Sci.*, *11*, 1633–1644.
Pendergrass, A. G., and D. L. Hartmann (2014a), The atmospheric energy constraint on global-mean precipitation change, *J. Clim.*, *27*, 757–768.
Pendergrass, A. G., and D. L. Hartmann (2014b), Two modes of change of the distribution of rain, *J. Clim.*, *27*, 8357–8371.
Pendergrass, A. G., and D. L. Hartmann (2014c), Changes in the distribution of rain frequency and intensity in response to global warming, *J. Clim.*, *27*, 8372–8383.
Polade, S. D., D. W. Pierce, D. R. Cayan, A. Gershunov, and M. D. Dettinger (2014), The key role of dry days in changing regional climate and precipitation regimes, *Nat. Sci. Rep.*, *4*, 4364, 1–8.
Pritchard, M. S., and C. S. Bretherton (2014), Causal evidence that rotational moisture advection is critical to the superparameterized Madden–Julian oscillation, *J. Atmos. Sci.*, *71*, 800–815.
Pritchard, M. S., and R. C. J. Somerville (2009a), Assessing the diurnal cycle of precipitation in a multi-scale climate model, *J. Adv. Model. Earth Syst.*, *1*, 12, 1–16, doi:10.3894/JAMES.2009.
Pritchard, M. S., and R. C. J. Somerville (2009b), Empirical orthogonal function analysis of the diurnal cycle of precipitation in a multi-scale climate model, *Geophys. Res. Lett.*, *36*, L05812, doi:10.1029/2008GL036964.
Pritchard, M. S., M. W. Moncrieff, and R. C. J. Somerville (2011), Orogenic propagating precipitation systems over the United States in a global climate model with embedded explicit convection, *J. Atmos. Sci.*, *68*(8), 1821–1840.
Pritchard, M. S., C. S. Bretherton, and C. A. DeMott (2014), Restricting 32-128 km horizontal scales hardly affects the MJO in the Superparameterized Community Atmosphere Model v.3.0 but the number of cloud-resolving grid columns constrains vertical mixing, *J. Adv. Model. Earth Syst.*, *6*, 723–739, doi:10.1002/2014MS000340.
Ramirex, J. A., and S. U. S. Senarath (2000), A statistical–dynamical parameterization of interception and land surface–atmosphere interactions, *J. Clim.*, *13*, 4050–4063.
Randall, D., M. Khairoutdinov, A. Arakawa, and W. Grabowski (2003), Breaking the cloud parameterization deadlock, *Bull. Am. Meteorol. Soc.*, *84*(11), 1547–1564.
Rasch, P. J., M. J. Stevens, L. Ricciardulli, A. Dai, A. Negri, R. Wood, B. A. Boville, B. Eaton, and J. J. Hack (2006), A characterization of tropical transient activity in the CAM3 atmospheric hydrologic cycle, *J. Clim.*, *19*, 2222–2242.
Raymond, D. J., and A. M. Blyth (1992), Extension of the stochastic mixing model to cumulonimbus clouds, *J. Atmos. Sci.*, *49*(21), 1968–1983.
Richter, J. H., and P. J. Rasch (2008), Effects of convective momentum transport on the atmospheric circulation in the Community Atmosphere Model, version 3, *J. Clim.*, *21*, 1487–1499.
Rosa, D., and W. D. Collins (2013), A case study of sub-daily simulated and observed continental convective precipitation: CMIP5 and multiscale global climate models comparison, *Geophys. Res. Lett.*, *40*, 5999–6003, doi:10.1002/2013GL057987.
Rossow, W. B., A. Mekonnen, C. Pearl, and W. Goncalves (2013), Tropical precipitation extremes, *J. Clim.*, *26*, 1457–1466.
Seager, R., N. Naik, and G. A. Vecchi (2010), Thermodynamic and dynamic mechanisms for large-scale changes in the hydrological cycle in response to global warming, *J. Clim.*, *23*, 4651–4668.
Seneviratne, S. I., T. Corti, E. L. Davin, M. Hirschi, E. B. Jaeger, I. Lehner, B. Orlowsky, and A. J. Teuling (2010), Investigating soil moisture–climate interactions in a changing climate: A review, *Earth Sci. Rev.*, *99*, 125–161.
Smith, R. D., et al. (2010), The parallel ocean program (POP) reference manual, *Tech. Rep. LAUR-10-01853*, 140 pp., Los Alamos Natl. Lab., Los Alamos, NM.
Stan, C., and L. Xu (2014), Climate simulations and projections with a super-parameterized climate model, *Environ. Modell. Software*, *60*, 134–152.

Stan, C., M. Khairoutdinov, C. A. DeMott, V. Krishnamurthy, D. M. Straus, D. A. Randall, J. L. Kinter III, and J. Shukla (2010), An ocean-atmosphere climate simulation with an embedded cloud resolving model, *Geophys. Res. Lett.*, *37*, L01702, doi:10.1029/2009GL040822.

Stephens, G. L., and T. D. Ellis (2008), Controls of global-mean precipitation increases in global warming GCM experiments, *J. Clim.*, *21*, 6141–6155.

Stocker, T. F., D. Qin, G.-K. Plattner, M. Tignor, S. K. Allen, J. Boschung, A. Nauels, Y. Xia, V. Bex, and P. M. Midgley (Eds.) (2013), Climate change 2013: The physical science basis, in *Contribution of Working Group I to the Fifth Assessment Report of the Intergovernmental Panel on Climate Change*, Cambridge Univ. Press, Cambridge, U. K.

Sun, Y., S. Solomon, A. Dai, and R. W. Portmann (2006), How often does it rain?, *J. Clim.*, *19*, 916–934.

Sun, Y., S. Solomon, A. Dai, and R. W. Portmann (2007), How often will it rain?, *J. Clim.*, *20*, 4801–4818.

Susskind, J., P. Piraino, L. Rokke, L. Iredell, and A. Mehta (1997), Characteristics of the TOVS pathfinder path A dataset, *Bull. Am. Meteorol. Soc.*, *78*, 1449–1472.

Tan, J., C. Jakob, W. B. Rossow, and G. Tselioudis (2015), Increases in tropical rainfall driven by changes in frequency of organized deep convection, *Nature*, *519*, 451–454.

Tao, W.-K., et al. (2009), The Goddard multi-scale modeling system with unified physics, *Ann. Geophys.*, *27*, 3055–3064.

Taylor, K. E., R. J. Stouffer, and G. A. Meehl (2012), An overview of CMIP5 and the experiment design, *Bull. Am. Meteorol. Soc.*, *93*, 485–498.

Trenberth, K. E. (2011), Changes in precipitation with climate change, *Clim. Res.*, *47*, 123–138.

Trenberth, K. E., A. Dai, R. M. Rasmussen, and D. B. Parsons (2003), The changing character of precipitation, *Bull. Am. Meteorol. Soc.*, *84*, 1205–1217.

Tulich, S. N. (2015), A strategy for representing the effects of convective momentum transport in multiscale models: Evaluation using a new superparameterized version of the Weather Research and Forecast model (SP-WRF), *J. Adv. Model. Earth Syst.*, *7*, 938–962, doi: 10.1002/2014MS000417.

Wang, M., et al. (2011), The multi-scale aerosol-climate model PNNL-MMF: Model description and evaluation, *Geosci. Model Dev.*, *4*(1), 137–168.

Watterson, I., and M. Dix (2003), Simulated changes due to global warming in daily precipitation means and extremes and their interpretation using the gamma distribution, *J. Geophys. Res.*, *108*(D13), 4379, doi:10.1029/2002JD002928.

Wolff, D. B., and B. L. Fisher (2009), Assessing the relative performance of microwave-based satellite rain-rate retrievals using TRMM ground validation data, *J. Appl. Meteorol. Climatol.*, *48*(6), 1069–1099.

Yang, Q., L. R. Leung, S. A. Rauscher, T. D. Ringler, and M. A. Taylor (2014), Atmospheric moisture budget and spatial resolution dependence of precipitation extremes in aquaplanet simulations, *J. Clim.*, *27*, 3565–3581.

Zhang, G. J., and N. A. McFarlane (1995), Sensitivity of climate simulations to the parameterization of cumulus convection in the Canadian climate center general-circulation model, *Atmos. Ocean*, *33*(3), 407–446.